Quantum computing with quantum dots on quantum linear supports

K. R. Brown, D. A. Lidar,* and K. B. Whaley

Department of Chemistry, University of California, Berkeley, California 94720-1460
(Received 22 May 2001; published 11 December 2001)

Motivated by the recently demonstrated ability to attach quantum dots to polymers at well-defined locations, we propose a condensed-phase analog of the ion-trap quantum computer: a scheme for quantum computation using chemically assembled semiconductor nanocrystals attached to a linear support. The linear support is either a molecular string (e.g., DNA) or a nanoscale rod. The phonon modes of the linear support are used as a quantum-information bus between the dots. Our scheme offers greater flexibility in optimizing material parameters than the ion-trap method, but has additional complications. We discuss the relevant physical parameters, provide a detailed feasibility study, and suggest materials for which quantum computation may be possible with this approach. We find that Si is a potentially promising quantum-dot material, already allowing a $5-10$-qubit quantum computer to operate with an error threshold of 10^{-3}.

I. INTRODUCTION

The tremendous excitement following the discovery of fast quantum algorithms [1,2] has led to a proliferation of quantum computer proposals, some of which have already been realized in a rudimentary fashion. A representative list includes nuclear spins in liquids [3–5] and solids [6], trapped ions [7–10], atoms in microwave cavities [11], atoms in optical lattices [12], atoms in a photonic band-gap material [13–15], quantum dots [16–24], donor atoms in silicon [25,26] and silicon-germanium arrays [27], Josephson junctions [28–32], electrons floating on helium [33], electrons transported in quantum wires [34,35], quantum optics [36,37], quantum Hall systems [38], and anyons [39,40]. For critical reviews of some of these proposals see [41–43]. To date, no single system has emerged as a clear leading candidate. Each proposal has its relative merits and flaws with respect to the goal of finding a system, which is both scalable and fault tolerant [44] and is at the same time technically feasible. In this paper we examine the possibility of making a solid-state analog of a scheme originally proposed for the gas phase, namely, trapped ions. One purpose of conducting such a study is to undertake a critical assessment of both the benefits and the disadvantages, which arise on translation of an architecture designed for atomic states coupled by phonons to the corresponding architecture for condensed-phase qubits. Our proposal uses quantum dots (semiconductor nanocrystals) and quantum linear supports (polymers or nanorods) in an ultracold environment. It relies on recent advances in the ability to chemically attach nanocrystals to polymers in precisely defined locations. Quantum dots are coupled through quantized vibrations of the linear support that are induced by off-resonance laser pulses, and information is stored in the exciton states of the dots. Internal operations on exciton states are accomplished using Raman transitions. We provide here a detailed analysis that allows evaluation of the merits and demerits of a condensed-phase

rather than gas-phase implementation.

Semiconductor nanostructures are known as "quantum dots" (QDs) when their size is of the order of or less than the bulk-exciton Bohr radius. In such "zero-dimensional" QDs the electron-hole pairs are confined in all three dimensions and the translational symmetry that holds for bulk semiconductors is totally lost. As a result of this quantum confinement the energy-level continuum of the bulk material changes into a discrete-level structure. This structure is very sensitively dependent on the QD radius and shape, crystal symmetry, relative dielectric constant (compared to the surrounding medium), surface effects, and defects. This sensitivity can be used to create and control a wide range of optical effects [45]. In general, the term "quantum dot" is used to refer to both "zero-dimensional" semiconductor structures embedded within or grown on a larger lattice, i.e., lattice bound, *and* to individual, chemically assembled semiconductor nanocrystals [46]. QDs can be created in a larger crystal structure by confining a two-dimensional electron gas with electrodes [47], or by making interface fluctuations in quantum wells [48]. A number of promising proposals for quantum computation have been made using the lattice-bound dots [16–22]. We consider here instead the chemically assembled semiconductor nanocrystals. In the remainder of this paper the term QD will therefore be implicitly understood to refer specifically to chemically assembled nanocrystals.

A large amount of theoretical and experimental information about nanocrystal QDs exists. Nanocrystals have been studied for their photoluminescence properties, linear absorption properties, and nonlinear spectroscopy using a variety of models and techniques [49–85]. For reviews see, e.g., [86–88]. These studies clarified the roles of size-dependence, lattice structure, surface effects, and environment on the exciton spectrum. However, little attention has been paid so far to the possibility of using nanocrystal QDs for quantum computing. One reason may be the difficulty of coupling nanocrystals. Direct interactions between separate dots are small and difficult to engineer, so that the route to scalability is not obvious. In the only other study to date that proposed to use nanocrystals for quantum computing, Brun

*Present address: Department of Chemistry, University of Toronto. 80 St. George Street, Toronto, Ontario M5S 3H6.

and Wang considered a model of nanocrystals attached to a high-Q microsphere and showed that the interaction between QDs can be achieved by using whispering-gallery modes of the microsphere to entangle individual qubits [23]. One problem with the realization of this model is that only a few QDs can be placed on each microsphere. Therefore, scalability would depend on the ability to connect the microspheres by optical wires.

An exciting route to bypass the coupling problem for quantum dots is suggested by the recently demonstrated ability to attach QDs to polymers by chemical methods at well-defined locations [89]. We show below that at sufficiently low temperatures, the QD-polymer system has quantized vibrational modes that can be used to couple electronic excitations in quantum dots in a controlled and coherent manner. This "quantum-information bus" concept derives from the ion-trap implementation of quantum computation proposed by Cirac and Zoller [7]. Ion-trap schemes take advantage of addressable multilevel ions that are trapped in harmonic wells. The ions are then coupled through interaction with their collective vibrational modes [7].[1] This scheme can be extended to any system of multilevel quantum objects bound by coupled quantum harmonic oscillators. We apply this approach here to a series of nanocrystal QDs attached to a linear support. The excitonic states of the QD act as carriers of quantum information, which are coupled to the vibrational states of the linear support. A linear support is a one-dimensional material (e.g., a stretched polymer or a clamped nanoscale rod) that is connected at each end to a wall. The support is contained in either a vacuum or a noninteracting condensed-phase matrix such as liquid helium. Although quantized acoustic-phonon modes have not yet been detected in nanoscale supports, low-temperature studies have started to probe the quantum properties of such systems, e.g., the quantum of thermal conductance [109].

The main advantage of using quantum dots rather than ions is the ability to control the optical properties of quantum dots by varying the size, shape, and composition of the dot. On the other hand, a disadvantage is that the analysis for quantum dots is complicated by the fact that they are complex composite objects and are not naturally "clean." For example, defects and surface effects can influence the electronic properties [90]. Our model presupposes that nanocrystals that are sufficiently "clean" will ultimately be available, so this puts some severe demands on the experimentalist.

Section II gives an outline of the proposal, describing the basic physics and the formal similarities with the ion-trap scheme. Section III describes the physics of the qubits, namely, the electronic states of quantum dots and the quantum linear support that provides the information bus between qubits. A summary of the necessary requirements of the qubit states is given here. In Sec. IV we then show how one-qubit and two-qubit operations can be performed in this system of coupled quantum dots. Section V discusses the *feasibility* of

---

[1]In the original Cirac-Zoller proposal [7] the ions are coupled using the motional ground state, but it was shown later that this requirement can be relaxed [10].
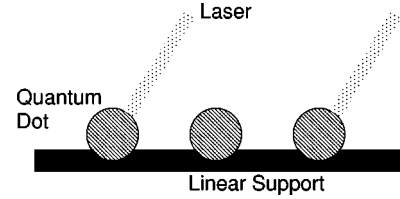

FIG. 1. Schematic visualization of N quantum dots attached to a linear support composed of a nanoscale rod or molecular string. Each quantum dot is addressed by a different laser. The absorption of the dots can be tuned by varying their sizes, allowing selective addressability with lasers of different wavelengths.

undertaking quantum logic, with a detailed analysis of the constraints imposed by decoherence and physical parameters. Quantitative estimates are made for several specific candidate systems in Sec. VI, followed by conclusions and discussion in Sec. VII.

II. THEORETICAL OVERVIEW

We outline here the basic elements of the quantum-dot–quantum-linear-support scheme for quantum computation. The proposed system consists of semiconductor nanocrystal QDs attached at spacings of several tens of nanometers to a quantum linear support (a string or rod). Each QD supports one qubit through a certain choice of excitonic states. Single-qubit operations are executed by optical transitions between these states. QDs are coupled by the linear support in analogy to the ion-trap scheme [7]. Thus, one uses detuned laser pulses to excite a phonon of the quantum linear support, which can then be used to cause conditional interactions between different dots. The system is depicted schematically in Fig. 1. The distance between the quantum dots is assumed to be large relative to their size (see also Secs. III B and III C.) For identical QDs, the QDs need to be separated by a distance larger than the laser-beam waist to guarantee that the QDs can be individually addressed. For typical QD excitation energies, the diffraction-limited-beam waist will be of the order of microns, so the separtion between the QDs will be larger than this. In the presence of external driving fields, the full Hamiltonian can be written as the sum of three contributions

$$H = H_0 + H_C + H_I,$$

where H_0 is the free Hamiltonian, H_C is the coupling Hamiltonian, and H_I is the Hamiltonian describing the interaction between the system and the applied laser fields.

The free Hamiltonian H_0 is given by

$$H_0 = \sum_{n=1}^{N} \sum_j \hbar \omega_{nj}^e |\Psi_j\rangle_n \langle\Psi_j| + \sum_{n=1}^{N} \sum_k \hbar \omega_{nk}^d b_{nk}^\dagger b_{nk}$$

$$+ \sum_m \hbar \omega_m^s a_m^\dagger a_m + \sum_l \hbar \omega_l^f c_l^\dagger c_l. \tag{1}$$

These four terms represent the energies of the excitons, QD phonons, linear-support phonons, and external electromagnetic field, respectively. Here n is the QD index, $|\Psi_j\rangle_n$ is an

exciton eigenstate in the nth QD, b_{nk} is an annihilation operator of the kth phonon mode of the nth QD, a_m is an annihilation operator of the mth linear-support phonon mode, and c_l is an annihilation operator of the lth mode of the quantized external electromagnetic field. The phonon frequencies of the support are denoted by ω^s, and those of the quantum dot by ω^d.

The coupling Hamiltonian H_C is given by

$$H_C = \sum_{njkl} \beta_{njkl} |\Psi_j\rangle_n \langle \Psi_k | c_l^\dagger + \sum_{njkl} \gamma_{njik} |\Psi_j\rangle_n \langle \Psi_i | b_{nk}^\dagger$$

$$+ \sum_{njkl} \alpha_{nkl} b_{nk} c_l^\dagger + \text{H.c.} \qquad (2)$$

The first term is responsible for radiative decay of exciton states. The most important radiative-decay pathway is the recombination of the electron and the hole. The second term describes the exciton-phonon interaction and gives rise to both pure dephasing and nonradiative transitions between exciton states. The third term is a coupling between the QD phonons and the electromagnetic field.

The interaction Hamiltonian H_I describes the coupling of the excitons to single-mode plane-wave lasers in a standing-wave configuration. Standing-wave lasers are not requisite for our proposal, but they allow for both faster and more reliable operations as discussed in Sec. V B. We treat the laser fields semiclassically. In the dipole limit, we can write

$$H_I = \mathbf{D} \cdot \mathbf{E} = \sum_{kijn} [_n\langle \Psi_i | e(\mathbf{r}_e^n - \mathbf{r}_h^n) | \Psi_j \rangle_n |\Psi_i\rangle_n \langle \Psi_j |] \cdot [\epsilon_\mathbf{k} E_\mathbf{k}$$

$$\times \sin(\mathbf{k} \cdot \mathbf{r}_{cm}^n + \phi_x) \cos(\nu_\mathbf{k} t - \phi_t)]. \qquad (3)$$

Here $\mathbf{r}_e^n$ and $\mathbf{r}_h^n$ are the position vectors of the electron and hole in the nth QD, respectively; $\mathbf{r}_{cm}^n$ is the center of mass location of this QD; $\epsilon_\mathbf{k}$, $E_\mathbf{k}$, and $\nu_\mathbf{k}$ are, respectively, the polarization, electric-field amplitude, and frequency associated with the field mode $\mathbf{k}$; ϕ_x and ϕ_t are the spatial and temporal phases of the field. The dipole limit is valid here since a typical energy scale for single-particle electronic excitations in QDs is $0.1-1$ eV, corresponding to wavelengths $1/k \sim 0.1-1$ μm. For a typical dot radius $R \leqslant 5$ nm, the electric field is then almost homogeneous over the dot. In analogy to ion-trap schemes [7], the center of mass of the nth QD, $\mathbf{r}_{cm}^n$, is decomposed into its constituent phonon modes,

$$\mathbf{r}_{cm}^n = \sum_m c_{mn} \mathbf{q}_m = \sum_m c_{mn} \mathbf{q}_{0m}(a_m^\dagger + a_m), \qquad (4)$$

where $\mathbf{q}_m$ are normal modes and $\mathbf{q}_{0m}$ is the zero-point displacement for the mth normal mode; $|\mathbf{q}_{0m}| = \sqrt{\hbar/2M\omega_m}$, where M is the mass of the mode and ω_m is the mode frequency. For low-phonon occupation numbers, where the motion of the center of mass of the QD is small compared to the wavelength of the light, the Lamb-Dicke regime is obtained, i.e.,

$$\eta_{mn\mathbf{k}} = \mathbf{k} \cdot c_{mn} \mathbf{q}_{0m} \ll 1. \qquad (5)$$

Therefore, we can expand H_I to first order in the Lamb-Dicke parameter η,

$$H_I = 2\hbar \sum_{\mathbf{k}ijn} g_\mathbf{k}^{ijn} |\Psi_i\rangle_n \langle \Psi_j | \cos(\nu_\mathbf{k} t - \phi_t) \Big[\sin\phi_x$$

$$+ \sum_m \eta_{mn\mathbf{k}}(a_m^\dagger + a_m)\cos\phi_x \Big]. \qquad (6)$$

Here

$$g_\mathbf{k}^{ijn} = {}_n\Big\langle \Psi_i \Big| \frac{eE_\mathbf{k}}{2\hbar} \epsilon_\mathbf{k} \cdot (\mathbf{r}_e^n - \mathbf{r}_h^n) \Big| \Psi_j \Big\rangle_n \qquad (7)$$

is the resulting coupling parameter between the carrier states in the nth QD. The second term in Eq. (6) transfers momentum from the laser field to the QD, thereby exciting phonon modes of the linear support. This term allows us to perform two-qubit operations as described below. Manipulation of the spatial phase ϕ_x allows us to selectively excite either the carrier transition, i.e., a change in the internal degrees of freedom of the QD without changing the vibrational state of the support ($\Phi_x = \pi/2$), or a sideband transition in which the internal degrees of freedom of both the QD and the vibrational mode of the support are changed ($\Phi_x = 0$), depending on whether our QD is located at the antinode or node of the laser, respectively [9].

Now, let $\Omega = 2\pi/\tau_{op}$ be the Rabi frequency of our desired quantum operations [see Sec. IV] and let T be the temperature. Our system must then satisfy the following set of basic requirements.

(1) $\tau_{op} < \tau_{rec}$, where τ_{rec} is the time scale for exciton recombination. Typically $\tau_{rec} = 10^{-3} - 10^{-6}$ s [60,91].

(2) $\Omega < \omega_1^s$, where ω_1^s is the first harmonic of the linear-support spectrum. This requirement must be met in order to resolve the individual support modes.

(3) $k_b T < \hbar \omega_1^s$. This ensures that only the ground-state phonon mode is occupied. This requirement comes from the Cirac-Zoller ion-trap scheme [7], where the motional ground state is used as the information bus.

(4) Dephasing and population transfer due to exciton-phonon coupling must be minimized, or preferably avoided altogether.

We now discuss the details of our system in light of these requirements.

III. QUBIT AND LINEAR SUPPORT DEFINITIONS

A. Definition of qubits

In analogy to the Cirac-Zoller ion-trap scheme [7], three excitonic states will be used, denoted $|0\rangle_n, |1\rangle_n$, and $|2\rangle_n$. Advances in ion-trap methodology have allowed this requirement to be reduced to only two states [92,93,10]. However, for our purposes it suffices to use the more familiar three-state scheme. The states $|0\rangle_n$ and $|1\rangle_n$ are the qubit logic states, and $|2\rangle_n$ is an auxiliary state that is used when performing two-qubit operations. These three-exciton states must possess the following properties.

(1) The states should be dark for optical recombination: This is required so that we will have long recombination lifetimes.

(2) The states should be dark for radiative relaxation to other exciton states: This is required to prevent leakage to other exciton states.

(3) The states should be degenerate: The energy separation is required to be smaller than the lowest-energy internal phonon, in order to suppress nonradiative transitions between states. We wish to make transitions between vibronic eigenstates, rather than creating oscillating wave packets, which would dephase as they move on different potential surfaces. Obtaining a large amplitude for moving between vibrational eigenstates of two surfaces depends on the existence of two features, (i) large Frank-Condon overlap [94] between these eigenstates, which will be the case for degenerate exciton potential-energy surfaces; (ii) very narrow bandwidth laser pulses, which can selectively address the required states. These transitions are described in Sec. IV A. The degeneracy will need to be broken in order to perform certain operations.

In order to choose states that satisfy the above requirements, detailed calculation of the exciton wave functions and fine structure of the quantum dots is essential. We employ here the multiband effective-mass model that has been employed by a number of groups for calculation of the band-edge exciton fine structure in semiconductor QDs made of direct-band-gap semiconductors [52,60]. For larger nanocrystals, possessing radii $R > 20$ Å, the multiband effective-mass theory is generally in reasonably good agreement with experiment as far as energetics are concerned [73]. It has been used extensively for CdSe nanocrystals by Efros and co-workers [61]. While the effective-mass approximation (EMA) has known serious limitations [87], and has been shown not to provide quantitative results for smaller nanocrystals [73], it nevertheless provides a convenient, analytically tractable description, with well-defined quantum numbers for individual states, and will allow us to perform an order-of-magnitude assessment of the feasibility of our scheme.

To explain the exciton-state classification resulting from the multiband EMA, it is necessary to consider a hierarchy of physical effects leading to an assignment of appropriate quantum numbers. These effects are, in decreasing order of importance, (i) quantum confinement (dot of finite radius, typically smaller than the bulk-exciton radius), (ii) discrete lattice structure (iii) spin-orbit coupling, (iv) nonspherical nanocrystal geometry and facetting of surfaces, (v) lattice anisotropy (e.g., hexagonal lattice), and (vi) exchange coupling between electron and hole spin. The electron-hole Coulomb interaction is neglected: detailed calculations show that this may be treated perturbatively over the range of nanocrystal sizes for which the EMA is accurate [77,95]. These effects lead to the following set of quantum numbers: n_e (n_h) the principle electron (hole) quantum number, J_e (J_h) the total electron (hole) angular momentum, L_e (L_h) the lowest angular momentum of the electron (hole) envelope wave function, S_e (S_h) the electron (hole) Bloch total angular momentum, and the total angular momentum projection

$$F_z = m_K + m_s, \qquad (8)$$

where $m_K = \pm 1/2, \pm 3/2, \pm 5/2, \dots$ refers to the projection of the hole total angular momentum J_h, and $m_s = \pm 1/2, \pm 3/2, \pm 5/2, \dots$ is the projection of the electron total angular momentum J_e. State multiplets are classified by $n_e L_{e J_e} n_h L_{h J_h}$, e.g., $1S_{1/2} 1P_{3/2}$, and states within the multiplet are labeled by F_z. For a II-VI semiconductor such as CdSe, the Bloch states for the valence-band hole states possess total angular momentum $S_h = 3/2, 1/2$, derived from coupling of the local orbital angular momentum 1 in p orbitals with hole spin 1/2. The corresponding Bloch states for the conduction-band electron states have total angular momentum $S_e = 1/2$, derived from coupling of the local orbital angular momentum 0 in s orbitals, with electron spin 1/2. We consider here only states within the band-edge multiplet, for which $L_e = L_h = 0$ and $S_e = 1/2, S_h = 3/2$. Hence the total electron and hole angular momenta are given by $J_e = 1/2, J_h = 3/2$, respectively, and there are a total of eight states within this multiplet. It follows from Eq. (8) that there is one $F_z = 2$ state, two $F_z = 1$ states, two $F_z = 0$ states, two $F_z = -1$ states, and one $F_z = -2$ state in this $1S_{1/2} 1S_{3/2}$ multiplet. States within a doublet are distinguished by a superscript (L or U). The eigenfunctions, linear absorption spectrum, and selection rules for dipole transitions from the ground state to this lowest-lying EMA multiplet are calculated in Ref. [60]. For spherical QDs the following results were found.

(1) Hexagonal crystal structure: The $F_z = \pm 2$ states constitute degenerate exciton ground states. The $F_z = \pm 2$ states and one of the $F_z = 0$ states (denoted 0^L) are optically dark in the dipole approximation.

(2) Cubic crystal structure: The $F_z = 0^L, \pm 1^L, \pm 2$ states constitute degenerate exciton ground states and are all optically dark.

We consider here explicitly a nanocrystal made from a direct-band-gap material with cubic crystal structure. An exciton wave function of the $1S_{1/2} 1S_{3/2}$ multiplet, $\Psi_{F_z}(\mathbf{r}_e, \mathbf{r}_h)$, can be expanded in terms of products of single-particle wave functions $\psi^S_{1/2, m_s}(\mathbf{r}_e)$ and $\psi^S_{3/2, m_K}(\mathbf{r}_h)$ [52,60]. In order to satisfy the requirement of optically dark qubits [recall condition (1) above], we construct our qubit from the $F_z = -2, 0^L$ states,

$$|0\rangle \equiv |\Psi_{0^L}(\mathbf{r}_e, \mathbf{r}_h)\rangle = \frac{1}{\sqrt{2}} [|\psi^S_{1/2, -1/2}(\mathbf{r}_e) \psi^S_{1/2, +1/2}(\mathbf{r}_h)\rangle$$

$$- |\psi^S_{1/2, +1/2}(\mathbf{r}_e) \psi^S_{3/2, -1/2}(\mathbf{r}_h)\rangle],$$

$$|1\rangle \equiv |\Psi_{-2}(\mathbf{r}_e, \mathbf{r}_h)\rangle = |\psi^S_{1/2, -1/2}(\mathbf{r}_e) \psi^S_{3/2, -3/2}(\mathbf{r}_h)\rangle. \qquad (9)$$

The auxiliary level for cycling transitions is taken to be the $F_z = 2$ state,

$$|2\rangle \equiv |\Psi_{+2}(\mathbf{r}_e, \mathbf{r}_h)\rangle = |\psi^S_{1/2, +1/2}(\mathbf{r}_e) \psi^S_{3/2, +3/2}(\mathbf{r}_h)\rangle. \qquad (10)$$

Explicit expressions for the electron and hole wave functions are given in the Appendix. The states $|0\rangle, |1\rangle, |2\rangle$ are degenerate and have equal parity [determined by $(-1)^{F_z}$].

Naturally, for nonspherical, noncubic, and/or indirect-band-gap materials, other states may be more appropriate. It is only essential that they satisfy the requirements above. In this paper we shall use primarily the EMA states described above for cubic nanocrystals of direct gap materials, because they illuminate in an intuitive and quantifiable manner the difficulties associated with our proposal. However, in the discussion of feasibility (Sec. V), we will also present results obtained with qubit states obtained from tight-binding calculations for nanocrystals constructed from an indirect-band-gap material (silicon).

B. Quantum linear support

In order to determine whether quantum computation is possible on such a system we need to examine also the properties of the linear support. The support is made out of K small units, e.g., unit cells or monomers. We can write the displacement of each unit as a sum of normal modes,

$$\mathbf{x}_k = \sum_m \tilde{c}_{mk}\mathbf{q}_m = \sum_m \tilde{c}_{mk}\mathbf{q}_{0m}(a_m^\dagger + a_m). \tag{11}$$

The zero-point displacements for a homogeneous support are

$$|\mathbf{q}_{0m}| = \sqrt{\hbar/(2\lambda l \omega_m)}, \tag{12}$$

where λ is the linear mass density and l is the length of the unit. The lowest-energy modes will be long-wavelength transverse modes. Since the wavelengths of the modes of interest are large compared to the separation between neighboring units, we can approximate the support as being continuous.

In many cases, a sparse number of attached QDs will have only a small effect on the normal modes of the support. The validity of this assumption depends on the materials chosen and will be discussed more thoroughly below. For now we will calculate all of the relevant properties assuming point-like, massless quantum dots consistent with our assumption that the spacing between the dots is larger relative to their intrinsic size. For the nth pointlike QD attached to unit cell k, with one dot per unit cell, we can identify the dot and cell normal-mode expansion coefficients. We then have $c_{mn} \equiv \tilde{c}_{mk}$, where $\tilde{c}_{mk}$ and c_{mn} are, respectively, the coefficients relating the displacement of the kth unit cell and nth QD to the displacement of the mth normal mode [Eqs. (4) and (11), respectively]. For a continuous support, the set of $\tilde{c}_{mk}$ becomes a function $\tilde{c}_m(x)$ that is the normalized solution to the wave equation on the support. Any specific value of c_{mn} can now be written $c_m(x_n)$, where x_n is the position of the nth QD.

The two most common types of linear continuous systems are strings and rods.

1. Strings

In a string, the resistance to transverse motion comes from an applied tension ϑ. The dispersion relation for the frequency of a string in mode m is

$$\omega_m^s = \sqrt{\frac{\vartheta}{\lambda}}k_m,$$

where λ is the linear mass density and k_m is the wave number. The normalized solution to the transverse wave equation with fixed ends is given by

$$c_m(x) = \sqrt{\frac{2l}{L}}\sin(k_m x),$$

where $k_m = m\pi/L$, l is the unit length, and L is the string length.

2. Rods

In a rod, the resistance to transverse motion results from internal forces. This leads to a different dispersion relation and, consequently, to a different solution $c_m(x)$. The transverse modes of a rod can be defined in terms of the length L, density ρ, Young's modulus Y, cross-sectional area A, and the second moment of A (or the massless moment of inertia of a slice of the rod), and $\mathbf{I}$. As shown by Nishiguchi et al. [96], the long-wavelength phonon modes ($\lambda \gtrsim 1000$ Å) are well described by the classical dispersion equation

$$\omega_m^s = k_m^2 \sqrt{\frac{YI_z}{\lambda A}},$$

where I_z is the moment in the direction of the displacement.

The transverse normal modes for a clamped rod are well known [97], resulting in the solution

$$c_m(x) = N_m[\sin(k_m L) - \sinh(k_m L)][\cos(k_m x) - \cosh(k_m x)]$$
$$- [\cos(k_m x) - \cosh(k_m x)][\sin(k_m L) - \sinh(k_m L)].$$

Here N_m is a normalization constant proportional to $\sqrt{1/L}$. The values of k_m are not known analytically, but can be shown to be proportional to $1/L$.

C. Approximations

The important parameters characterizing the support are ω_1^s, the frequency of its first harmonic, and the product

$$\mathbf{S}_{nm} \equiv c_{nm}\mathbf{q}_{0m}. \tag{13}$$

This product is the quantum-dot displacement resulting from the zero-point motion of mode m of the support. We shall refer to it as the *dot-modal displacement*. The above discussion of vibrations in the support assumed massless QDs, motivated by the assumption that they have negligible spatial extent relative to the distance between them. To investigate the effect of the finite mass of the quantum dots, we computed numerical solutions of the coupled vibration equations for strings and rods having finite-mass increments located at discrete points, simulating the attachment of finite mass quantum dots. These numerical calculations show that for sparsely spaced dots of mass small enough that the total weight is of the same order of magnitude as the weight of the support alone, the resulting value of S_{nm} remains unaffected
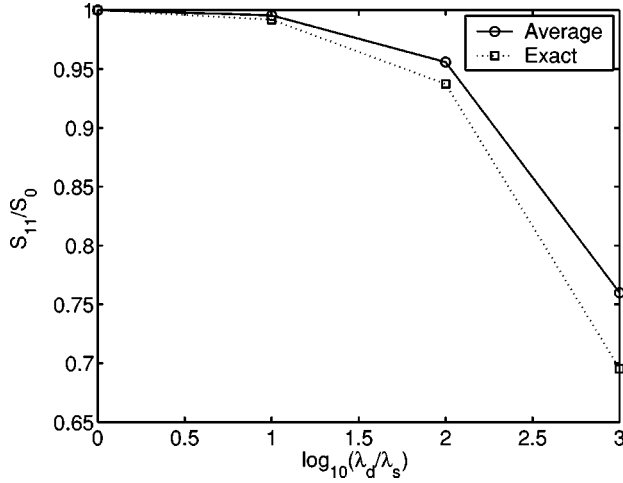
FIG. 2. The addition of a sparse number of quantum dots to the linear support has relatively little effect on the dot modal displacement S_{nm}. Here we present results for S_{11}, the dot displacement resulting from the first harmonic of the support, for a system with two QDs attached to a string of length $L = 2000$ nm. The QDs are centered at 499 and 1501 nm. Each QD is represented as an increased density that is distributed over a length of 2 nm, e.g., 499 ± 2 nm. Each dot experiences a displacement, which is affected by the addition of the second dot on the support. The dot displacement measured relative to the value obtained from a homogeneous string, S_0, is plotted as a function of $\log_{10}(\lambda_d/\lambda_s)$, where λ_d is the linear-density increment due to the dot and λ_s is the linear density of the string. The solid line guides the eye through the exact solution, the dotted line through the solutions obtained for a homogenous density equal to the average density. One sees that the value of S_{11} changes by less than a factor of 2 over a three orders of magnitude change in λ_d for a fixed λ_s.

to within a factor of 2 by the presence of the dots (see Fig. 2). A simple way to approximate the presence of the QDs and retain an analytic solution is then to replace the linear density of the support by the average combined linear density of QD and support.

Since we are interested here in order-of-magnitude estimates of feasibility, we will approximate $c_m(x_n)$ by $\sqrt{2l/L}$. This approximation corresponds to the maximum value of $c_m(x_n)$ for a string and to approximately the maximum value of $c_m(x_n)$ for a rod. Since the larger the dot displacement, the larger the coupling between dots, this means that our estimations of number of operations will be an upper bound.

These approximations combined with Eq. (5) yield the following equation for the Lamb-Dicke parameter:

$$\eta_{m'n\mathbf{k}_2} = \mathbf{k}_2 \cdot \mathbf{S}_{nm} = k_2 S_{nm} \cos\theta = k_2 \sqrt{\frac{\hbar}{M\omega_m}} \cos\theta, \quad (14)$$

where θ is the angle between the modal displacement and the direction of the laser beam, and M is the total support mass, $M = L\lambda$. Note the inverse power dependence on M in Eq. (14). We shall see in Sec. V B that the massive nature of the linear support and the resulting small value of the Lamb-Dicke parameter provides the major limitation for our system.

IV. QUBIT OPERATIONS

A. One-qubit operations: Coupling of dots to light

1. Derivation of the interaction Hamiltonian in the rotating-wave approximation

While dipole transitions in QDs are similar, in principle, to dipole transitions in atomic systems, the strong coupling to internal phonon modes adds an additional complexity. Consider the modifications of Eqs. (1)–(3) for a single QD *unattached* to a linear support, interacting with a single laser field with the QD located at the antinode of the field, i.e., with the $\sin(\mathbf{k} \cdot \mathbf{r}^n_{\text{c.m.}} + \phi_x)$ term in Eq. (3) vanishing. Thus, omitting the linear support term,

$$H = \sum_j \hbar\omega_j^e |\Psi_j\rangle\langle\Psi_j| + \sum_k \hbar\omega_k^d b_k^\dagger b_k$$

$$+ \sum_{ijk} \hbar\gamma_{jik} |\Psi_j\rangle\langle\Psi_i|(b_k^\dagger + b_k)$$

$$+ \sum_{ij} 2\hbar g_\mathbf{k}^{ij} |\Psi_i\rangle\langle\Psi_j| \cos(\nu_\mathbf{k} t - \phi_t).$$

We separate this Hamiltonian into two parts, H_0 and H_I,

$$H_0 = \sum_j \hbar\omega_j^e |\Psi_j\rangle\langle\Psi_j| + \sum_k \hbar\omega_k^d b_k^\dagger b_k$$

$$+ \sum_{jk} \hbar\gamma_{jjk} |\Psi_j\rangle\langle\Psi_j|(b_k^\dagger + b_k), \quad (15)$$

$$H_I = \sum_{i\neq j,k} \hbar\gamma_{jik} |\Psi_j\rangle\langle\Psi_i|(b_k^\dagger + b_k)$$

$$+ \sum_{ij} 2\hbar g_\mathbf{k}^{ij} |\Psi_i\rangle\langle\Psi_j| \cos(\nu_\mathbf{k} t - \phi_t). \quad (16)$$

The "free" Hamiltonian H_0 may be diagonalized by a displacement transformation. Let $D_k(\alpha)$ be the unitary displacement operator,

$$D_k(\alpha) \equiv e^{\alpha b_k^\dagger - \alpha^* b_k} = D_k(-\alpha)^\dagger.$$

The displaced phonon operator d_{jk} is defined as

$$d_{jk} \equiv D_k(-\alpha_{jk}) b_k D_k(\alpha_{jk}) = b_k + \alpha_{jk},$$

and satisfies standard boson commutation relations

$$[d_{jk},d_{j'k'}^\dagger]=\delta_{kk'},$$

$$[d_{jk},d_{j'k'}]=[d_{jk}^\dagger,d_{j'k'}^\dagger]=0.$$

Note that for real α_{jk} we have $\alpha_{jk}(b_k^\dagger+b_k)=d_{jk}^\dagger d_{jk}-\alpha_{jk}^2-b_k^\dagger b_k$. Letting $\alpha_{jk}\equiv\gamma_{jjk}/\omega_k^d$ and inserting a complete set of exciton states into Eq. (15), we find

$$H_0=\sum_j \hbar\omega_j^e|\Psi_j\rangle\langle\Psi_j|+\sum_k \hbar\omega_k^d\sum_j |\Psi_j\rangle\langle\Psi_j|$$
$$\times[b_k^\dagger b_k-\alpha_{jk}(b_k^\dagger+b_k)]$$
$$=\sum_j \hbar\omega_j^e|\Psi_j\rangle\langle\Psi_j|+\sum_{jk} \hbar\omega_k^d|\Psi_j\rangle$$
$$\times\langle\Psi_j|\left[d_{jk}^\dagger d_{jk}-\left(\frac{\gamma_{jjk}}{\omega_k^d}\right)^2\right].$$

The eigenstates of $d_{jk}^\dagger d_{jk}$ are labeled $|n_{jk}\rangle$, where $d_{jk}^\dagger d_{jk}|n_{jk}\rangle=n|n_{jk}\rangle$ and $\langle n_{jk}|m_{j'k'}\rangle=\delta_{kk'}F_{nmk}^{jj'}.^2$ The $F_{nmk}^{jj'}$ are Franck-Condon factors [94], describing the overlap of vibrational eigenstates between different excitonic states j and j'. We can then rewrite H_0 as

$$H_0=\sum_j \hbar\omega_j^{e+}|\Psi_j\rangle\langle\Psi_j|+\sum_{jk} \hbar\omega_k^d|\Psi_j\rangle\langle\Psi_j|d_{jk}^\dagger d_{jk},$$

where $\omega_j^{e+}=\omega_j^e-\Sigma_k(\gamma_{jjk}/\omega_k^d)^2$ is the renormalized electronic energy level.

We transform to the interaction picture defined by H_0: $\tilde H_I=\exp(iH_0t/\hbar)H_I\exp(-iH_0t/\hbar)$. To do so, it is useful to insert into this expression two complete sets of displaced oscillator states belonging to different excitonic states i and j,

$$I_i\times I_j=\oplus_k\sum_n |n_{ik}\rangle\langle n_{ik}|\times\oplus_{k'}\sum_m |m_{jk'}\rangle\langle m_{jk'}|$$

$$=\oplus_k\sum_{nm} |n_{ik}\rangle\langle m_{jk}|F_{nmk}^{ij}.$$

Changing variables from b_k to d_{jk} in Eq. (16), and transforming to the interaction picture now yields, after some standard algebra,

---

[2]Note that n refers here to the occupation quantum number of the internal phonon modes, not to the quantum-dot index.

$$\tilde H_I=e^{iH_0t/\hbar}H_Ie^{-iH_0t/\hbar}$$

$$=\sum_{i\neq j,l} \hbar\gamma_{jik}|\Psi_i\rangle\langle\Psi_j|e^{i\omega_{ij}^{e+}t}\otimes_{k\neq l}\sum_{n,m} F_{nmk}^{ij}|n_{ik}\rangle\langle m_{jk}|$$

$$\times e^{i\omega_k^d(n-m)t}\otimes_l\sum_{n',m'} F_{n'm'l}^{ij}\left\{-\frac{\gamma_{jjl}}{\omega_l^d}|n_{il}'\rangle\langle m_{jl}'|\right.$$

$$\times\exp[i\omega_l^d(n'-m')t]+\sqrt{m'+1}|n_{il}'\rangle\langle(m'+1)_{jl}|$$

$$\left.\times\exp[i\omega_l^d(n'-m'-1)t]\right\}+\sum_{ij} \hbar g_{\mathbf k}^{ij}|\Psi_i\rangle\langle\Psi_j|$$

$$\times\exp[-i(\nu_{\mathbf k}t-\omega_{ij}^{e+}t-\phi_t)]\otimes_k\sum_{n,m} F_{nmk}^{ij}|n_{ik}\rangle$$

$$\times\langle m_{jk}|e^{i\omega_k^d(n-m)t}+\text{H.c.,} \qquad (17)$$

where $\omega_{ij}^{e+}\equiv\omega_i^{e+}-\omega_j^{e+}$.

While this expression appears very complicated, it can be drastically simplified under certain reasonable assumptions. First, note that for single-qubit operations we need to consider only two exciton states $|\Psi_a\rangle$ and $|\Psi_b\rangle$. The first term in $\tilde H_I$ essentially describes nonradiative transitions between exciton states due to phonon emission. Under the assumption that the phonon modes are initially unoccupied, we can choose the states $|\Psi_a\rangle$ and $|\Psi_b\rangle$ such that they have a negligible propensity for nonradiative transitions, i.e., they are protected against single-phonon emission [recall condition (3). for "good" qubits in Sec. III A]. This means that we can effectively set all γ_{jik} to zero, thus eliminating the first term in $\tilde H_I$. This important simplification is treated in detail in Sec. V A below. Thus we are left with

$$\tilde H_I=\hbar g_{\mathbf k}^{ab}|\Psi_a\rangle\langle\Psi_b|\exp[i\phi_t-it(\nu_{\mathbf k}-\omega_{ab}^{e+})]$$

$$\otimes_k\sum_{n,m} F_{nmk}^{ab}|n_{ak}\rangle\langle m_{bk}|e^{i\omega_k^d(n-m)t}+\text{H.c.}$$

We then tune our laser on resonance such that $\nu_k=\omega_{ab}^{e+}$, and make sure that the laser spectral width is much smaller than the lowest quantum-dot phonon frequency, ω_1^d. This allows us to make the rotating-wave approximation (RWA), i.e., eliminate all terms that rotate faster than ω_1^d, which leads to

$$\tilde H_I=\hbar g_{\mathbf k}^{ab}|\Psi_a\rangle\langle\Psi_b|e^{i\phi_t}\otimes_k\sum_n F_{nnk}^{ab}|n_{ak}\rangle\langle n_{bk}|+\text{H.c.}$$
$$(18)$$

This RWA interaction Hamiltonian, Eq. (18), is very similar to the familiar two-level system Hamiltonian used extensively in atomic optics [98]. However, the strength of the interaction is modulated here by the Franck-Condon factors, F_{nnk}^{ab}. To allow the simplification of the Hamiltonian from Eq. (17) to Eq. (18) requires a judicious choice of laser intensities and states. In our scheme the occupation n of all phonon modes will be initially zero. Using Eq. (7), it is useful to then introduce the factor
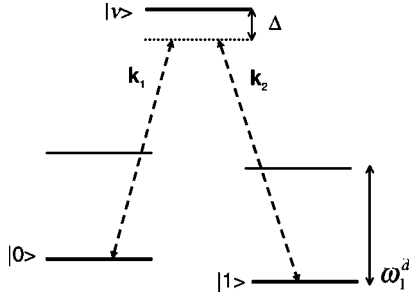
FIG. 3. Energy-level scheme for a quantum dot showing the laser fields and transitions necessary for one-qubit operations. (Energy-level spacings are not to scale.) Levels $|0\rangle$ and $|1\rangle$ constitute the qubit. The auxiliary level $|2\rangle$ is not involved in these transitions and is not shown. The linear support modes are not involved either. Two antinodal lasers, $\mathbf{k}_1$ and $\mathbf{k}_2$, allow us to perform a Raman transition via a virtual state $|v\rangle$. Transitions occur without changing internal phonon number, since the laser's frequency widths are smaller than the internal phonon frequency ω_1^d.

$$
\Omega_{\mathbf{k}}^{ab} = g_{\mathbf{k}}^{ab} \prod_k F_{00k}^{ab}
$$

$$
= \sqrt{\frac{2\pi\alpha I_{\mathbf{k}}}{\hbar}} \prod_k F_{00k}^{ab} \langle \Psi_a | \boldsymbol{\epsilon}_{\mathbf{k}} \cdot (\mathbf{r}_e - \mathbf{r}_h) | \Psi_b \rangle, \qquad (19)
$$

which corresponds to the Rabi frequency for an on-resonant transition between exciton states a and b. $I_{\mathbf{k}}$ is the laser intensity and $\alpha = e^2/(4\pi\varepsilon_0\hbar c)$ is the fine-structure constant.

2. Raman transitions

Since we wish to use near-degenerate states of equal parity for our qubits, we cannot employ dipole transitions. Hence we use Raman transitions. These connect states of equal parity via a virtual transition to a state with opposite parity. Recall that parity is determined by $(-1)^{F_z}$. Suppose we start in the $|1\rangle = |\psi_{1/2,-1/2}^S(\mathbf{r}_e)\psi_{3/2,-3/2}^S(\mathbf{r}_h)\rangle$ state, for which $F_z = -2$. We can then make transitions through a virtual level $|v\rangle$ that has opposite parity (e.g., $F_z = \pm 1$), to the state $|0\rangle$ having $F_z = 0$. Figure 3(a) provides a schematic of the coupled QD–laser-field system, showing the levels $|0\rangle$, $|1\rangle$, and $|v\rangle$ together with the fields required to cause a Raman transition. Under the assumptions that only two laser-field modes $\mathbf{k}_1$ and $\mathbf{k}_2$ are applied, and in the rotating-wave approximation, the standard theory of Raman transitions [99] leads to the following expression for the Raman-Rabi frequency between an initial state $|i\rangle$ and a final state $|f\rangle$:

$$
\Omega_{\text{Raman}}^{fi\mathbf{k}_2\mathbf{k}_1} = \frac{|\Omega_{\mathbf{k}_2}^{fj}\Omega_{\mathbf{k}_1}^{ji}|}{\Delta}. \qquad (20)
$$

Here k_1 and k_2 are chosen such that the detuning $\Delta = \omega_j - \omega_i - \nu_{\mathbf{k}_1} = \omega_j - \omega_f - \nu_{\mathbf{k}_2}$, j is the index of an intermediate exciton state chosen to provide a minimum value of Δ, and Ω_k^{ij} is defined in Eq. (19). For single-qubit transitions, both lasers are aligned such that the QD is positioned at antinodes.

For QDs possessing cubic crystal structure and composed of direct-band-gap materials, we have found it advantageous

to use the $F_z = 1$ and $F_z = -1$ states of the $1S_{1/2}1P_{5/2}$ multiplet as the intermediate state. An exciton wave function of the $1S_{1/2}1P_{5/2}$ multiplet $\Psi_{F_z}^v(r_e, r_h)$ can be expanded in terms of products of single-particle wave functions $\psi_{3/2,m_s}^S(r_e)$ and $\psi_{5/2,m_K}^P(r_h)$ [52,60]. The intermediate $F_z = \pm 1$ virtual states can be written as

$$
|\Psi_{\pm 1}^v(\mathbf{r}_e,\mathbf{r}_h)\rangle = -\frac{1}{\sqrt{3}}[\,|\psi_{1/2,\mp 1/2}^S(\mathbf{r}_e)\psi_{5/2,\pm 3/2}^P(\mathbf{r}_h)\rangle
$$
$$
+ \sqrt{2}|\psi_{1/2,\pm 1/2}^S(\mathbf{r}_e)\psi_{5/2,\pm 1/2}^P(\mathbf{r}_h)\rangle].
$$

The Raman-Rabi frequency Ω_{Raman} can then be adjusted by increasing the electric-field intensity and by reducing the detuning from the intermediate level. We will describe in detail in Sec. V B what range of values of intensity and detuning are allowed.

B. Two-qubit operations: Coupling quantum dots, quantum supports, and light

Our two-qubit operations are equivalent to those of the Cirac-Zoller scheme [7]. The use of optical Raman transitions to implement this scheme has been extensively explored [8]. In our case, we apply the Hamiltonian of Eq. (6) with two lasers k_1 and k_2 of frequency ν_1 and ν_2, respectively. For two-qubit operations, the quantum dot is centered at an antinode of k_1 and at a node of k_2. Switching to the interaction picture and calculating second-order transition probabilities to first order in η, one obtains the following effective Hamiltonian:

$$
H_{\text{eff}}^{nfi} = -\hbar \sum_m \eta_{mn\mathbf{k}_2}(a_m^\dagger e^{-i\omega_m t} + a_m e^{i\omega_m t})
$$
$$
\times \Omega_{\text{Raman}}^{fi\mathbf{k}_2\mathbf{k}_1}|\Psi_f\rangle_n\langle\Psi_i|e^{i(\omega_f - \omega_i)t}
$$
$$
\times \exp\{-i[(\nu_1 - \nu_2)t + \phi_2 - \phi_1]\} + \text{H.c.} \qquad (21)
$$

Note that the nodal and antinodal lasers result in an effective Hamiltonian in which η depends only on the nodal laser k_2. This differs from the effective Hamiltonian derived for Raman transitions when traveling waves are used [8]. The lasers are chosen to have a net red detuning, $\omega_f - \omega_i - \nu_1 + \nu_2 = -\omega_{m'}$. In the RWA (i.e., eliminating all terms rotating at $2\omega_m$), with $\phi_2 - \phi_1 = \pi$, this yields

$$
H_{\text{eff}}^{nfi} = \Omega_{nm'}^{fi\mathbf{k}_2\mathbf{k}_1}|\Psi_f\rangle_n\langle\Psi_i|a_{m'} + \text{H.c.}, \qquad (22)
$$

where

$$
\Omega_{nm'}^{fi\mathbf{k}_2\mathbf{k}_1} = \eta_{mn\mathbf{k}_2}\Omega_{\text{Raman}}^{fi\mathbf{k}_2\mathbf{k}_1}. \qquad (23)
$$

This combined QD-linear-support operation transfers the nth QD from state i to f, with an accompanying change of one quantum in the phonon mode m' of the support. A schematic representation of this operation for the qubit states $|\psi_i\rangle = |0\rangle$ and $|\psi_f\rangle = |1\rangle$ is shown in Fig. 4. Choosing interaction times such that $t = k\pi/(2\Omega_{nm'}^{fi\mathbf{k}_2\mathbf{k}_1})$, where k is an integer
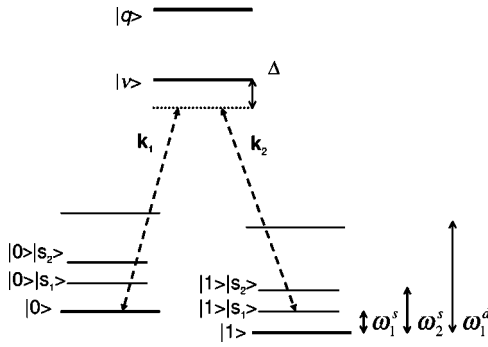
FIG. 4. Energy-level scheme for a quantum dot on the linear support showing laser fields necessary for implementation of two-qubit operations. As described in the text, the use of nodal and antinodal lasers allows us to selectively transfer population from $|0\rangle$ to the lowest-energy phonon sideband of $|1\rangle$ (labeled $|1\rangle|s_1\rangle$) via a Raman transition, without transferring population to the carrier. The minimum phonon frequency is denoted ω_1^s. Nonresonant transitions to higher-energy phonon sidebands ($|1\rangle|s_2\rangle$) constitute the main source of error in the proposed gates. For very high laser intensities, nonresonant quadrupolar transitions to higher-level states (represented by the state $|q\rangle$) also become important.

specifying the pulse duration, we can write the unitary operator $\exp(-[i/\hbar]H_{\mathrm{eff}}^{nfi}t) = U^{nfi}(t)$ as

$$U_k^{nfi} = \exp\left[-i\frac{k\pi}{2}(|\Psi_f\rangle_n\langle\Psi_i|a + \mathrm{H.c.})\right]. \quad (24)$$

In order for the Cirac-Zoller scheme to be successful, the phonon mode of interest, m, must start with zero occupation. The applied operations take advantage of the fact that the zero-occupation phonon state is annihilated by the lowering operator $a|0\rangle = 0$. The sequence of unitary operations $U_{C\text{-phase}} \equiv U_1^{n10}U_2^{n'20}U_1^{n10}$ then results in a controlled-phase operation between quantum dots n and n', i.e., it causes the second qubit n' to gain a phase of -1 if the first qubit n is in the $|1\rangle$ state, and no additional phase if the first qubit is in $|0\rangle$. This is equivalent to the matrix operator $I - 2|1\rangle_{n'}|1\rangle_{nn'}\langle1|_n\langle1|$. The time required to perform $U_{C\text{-phase}}$ is then $2\times(\pi/2)$ for ion n plus $1\times\pi$ for ion n', i.e.,

$$\tau_{C\text{-phase}} \equiv (\Omega_2^{nn'})^{-1} = \pi(\Omega_{nm'}^{fi\mathbf{k}_2\mathbf{k}_1})^{-1} + \pi(\Omega_{n'm'}^{fi\mathbf{k}_2\mathbf{k}_1})^{-1}. \quad (25)$$

Since the ions n and n' are identical we will use the approximation that $\Omega_{nm'}^{fi\mathbf{k}_2\mathbf{k}_1} \approx \Omega_{n'm'}^{fi\mathbf{k}_2\mathbf{k}_1}$ in the remainder of this work, hence

$$\Omega_2^{nn'} \approx \frac{1}{2\pi}\Omega_{nm'}^{fi\mathbf{k}_2\mathbf{k}_1} = \frac{1}{2\pi}\Omega_2. \quad (26)$$

The inverse of the average rate $\Omega_2^{nn'}$ can then be taken as a measure of the gate time, i.e., of the time for the two-qubit controlled-phase operation. We define Ω_2 as the sideband interaction strength

$$\Omega_2 \simeq \eta_{mn\mathbf{k}_2}\Omega_{\mathrm{Raman}}^{fi\mathbf{k}_2\mathbf{k}_1}. \quad (27)$$

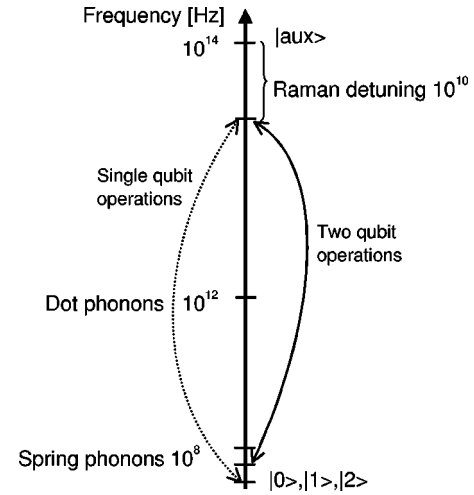

FIG. 5. Summary of energy scales involved in our proposal for single- and two-qubit operations. The states $|0\rangle$, $|1\rangle$, and $|2\rangle$ appear degenerate on the scale of this figure.

Calculation of $\Omega_{\mathrm{Raman}}^{fi\mathbf{k}_2\mathbf{k}_1}$ was described above in Sec. IV A [Eq. (20)]. We can obtain the Lamb14-Dicke parameter $\eta_{m'n\mathbf{k}_2}$ from the decomposition in Eq. (14). This now allows specific evaluation of the contribution from the linear support to the Lamb-Dicke parameter η. As described in Sec. III C, we approximate η as being independent of the specific dot and from now on will drop the dot index n.

C. Input and output

Since the qubit states do not include the ground state of the quantum dot, initialization will generally require a transformation from the ground state of no exciton to the defined qubit state. This can be accomplished by applying magnetic fields that will mix dark and light states allowing for optical transitions. If the magnetic field is then adiabatically removed, one is left with population in the dark exciton state only. Qubit measurements can be made by using a cycling transition, in analogy to ion traps [8].

We conclude this section by summarizing in Fig. 5 the relative energy scales involved in our proposal.

V. FEASIBILITY OF QUANTUM LOGIC

In this section we address in detail the question of the limitations imposed on our system by various physical constraints. We start by considering the issue of decoherence due to coupling of excitons to the internal nanocrystal phonon modes, and propose a solution to this problem. We then study the issues of scaling arising from the trade-off between massiveness of the support, laser intensity, and the need to maintain a large ratio of operations to exciton-recombination time. We find that the allowed size of our proposed quantum computer depends on the assumed threshold for fault-tolerant computation.

A. Decoherence

According to current analysis of experiments on nanocrystal quantum dots [100], exciton dephasing derives predominantly from the diagonal phonon-exciton coupling term of Eq. (2),

$$\sum_{j,k} |j\rangle\langle j| (\gamma_{kj}^* b_k^\dagger + \gamma_{kj} b_k). \tag{28}$$

Here γ_{kj} is the self-coupling of an exciton state j via phonon k, and b_k is the lowering operator for the kth phonon mode in the ground electronic state. In the ground state the coupling is zero, and all excited electronic states have potential-energy surfaces that are shifted with respect to this ground state. We desire to eliminate dephasing due to the first-order phonon-exciton interaction. In the typical experimental situations in which dephasing has been studied in the past, dephasing occurs on a time scale of nanoseconds for small dots [100]. This rate is extremely rapid compared to the experimental recombination time of dark states ($\sim 10^{-6}$ s for direct-band-gap materials such as CdSe [60]). The reason for such fast dephasing is twofold. First, the vibrational stationary state of the first electronic level becomes a moving vibrational wave packet on the upper electronic surface, because the spectral width of the pulse is too broad to distinguish vibrational eigenstates. Second, the QD is embedded in a solid-state medium where the vibrations of the nanocrystal are then coupled to vibrations of the larger lattice. The phonons of the QD can be treated as analogous to damped cavity modes in atomic optics [98]. In the case of strong coupling, one finds from numerical simulation that the dephasing between any two states j and j' is related to the rate of phonon-mode excitation. The latter is proportional to $|\gamma_{kj} - \gamma_{kj'}|^2$ for each mode k [100]. This conclusion of fast dephasing agrees with the analogous result for a leaky optical cavity [98] as well as with the results of experimental [101] and theoretical [100] analysis for embedded semiconductor nanocrystals.

The dephasing can be reduced in three ways. First, the coupling of the QD phonon modes to external phonon and photon modes can be reduced by a judicious choice of nanocrystal geometry and material. In our case the QD can dissipate phonon modes only to the support. In the limit of no coupling to external modes, there will be no dephasing but the time required for recurrences could limit our gate-repetition rate. Although the oscillations will be fast, the oscillations for different phonon energies will be incommensurate with one another. This could introduce a slow quantum beating between ground and excited electronic states, which would have the undesirable consequence of requiring gate durations to equal a full beat cycle.

Second, one can find a set of electronic states $|j\rangle$ such that

$$\gamma_{kj} - \gamma_{kj'} = 0 \quad \forall \ j,j' \ \text{and} \ \forall \ k. \tag{29}$$

Physically this condition represents a set of electronic states that create the same potential-energy surface for nuclear motion. This elimination of decoherence by degeneracy is an example of a decoherence-free subspace [102–104]. The Jahn-Teller effect implies that no two such states should ex-

ist, because there will always be a phonon mode that will distinguish between these states due to nonlinearity [105]. However, in the linear approximation we have

$$\gamma_{kj} = \langle j| \gamma_k(\mathbf{r}_h) + \gamma_k(\mathbf{r}_e) |j\rangle. \tag{30}$$

The deformation potential coupling operator $\gamma_k(r)$ is a function of the phonon modes and is expressed as

$$\gamma_k(\mathbf{r}) \equiv \gamma_{nlm}(\mathbf{r}) = E_d \boldsymbol{\nabla} \cdot \mathbf{u}_{nlm}(\mathbf{r}), \tag{31}$$

where E_d is the deformation potential and $u_{nlm}(r)$ is the coordinate representation of the normalized spheroidal phonon mode of level n with angular momentum l and projection m. Following Takagahara [100], the spheroidal modes can be written as

$$\mathbf{u}_{nlm}(\mathbf{r}) = \sqrt{\frac{\hbar}{2\rho\omega_{nlm}}} [p_{nl} \mathbf{L}_{lm}(h_{nl}\mathbf{r}) + q_{nl} \mathbf{N}_{lm}(k_{nl}\mathbf{r})], \tag{32}$$

where ρ is the nanocrystal density, ω_{nlm} is the frequency of the spherical phonon nlm, $L_{lm}(hr) = (1/h)\boldsymbol{\nabla}\Psi_{lm}(hr)$, $N_{lm}(kr) = (1/k)\boldsymbol{\nabla}\times\boldsymbol{\nabla}\times r\Psi_{lm}(kr)$, and $\Psi(kr) = j_l(kr)Y_l^m(\Omega)$. $j_l(r)$ is an lth-order spherical Bessel function, $Y_l^m(\Omega)$ is a spherical harmonic, k_n and h_n satisfy stress-free boundary conditions at the surface, and p_{nl}, q_{nl} are determined by normalization. One can then write

$$\gamma_{nlm}(\mathbf{r}) = -E_d \sqrt{\frac{\hbar}{2\rho\omega_{nlm}}} p_{nl} h_{nl} j_l(h_{nl}r) Y_l^m(\Omega). \tag{33}$$

For a cubic, direct-gap nanocrystal, the states $|j\rangle$ are states of well-defined angular momentum projection. Since the Y_l^m in Eq. (33) connects states with equal projection, the only phonon modes that can have nonzero matrix elements in Eq. (30) are those with $m=0$ [106]. The resulting matrix elements will be independent of the sign of the exciton angular momentum projection F_z [Eq. (8)], i.e., the $m=0$ phonon modes cannot distinguish between exciton states having F_z or $-F_z$. Therefore, in the linear approximation, the states $|\Psi_{-2}(r_e, r_h)\rangle$ and $|\Psi_2(r_e, r_h)\rangle$ will not dephase with respect to each other. Recall that we took these states as our qubit state $|1\rangle$ and auxiliary state $|2\rangle$ [Eqs. (9) and (10)].

Third, and most importantly, one can change the way in which transitions are made. In the above two situations, the motional wave packet of one electronic surface is transferred to another electronic surface without changing shape, i.e., the Franck-Condon approximation holds. However, such a transition requires either a broad laser or a fast excitation. This is not actually the regime of relevance here. The scheme outlined in this work requires selective excitations of sidebands whose energy separation is orders of magnitude smaller than the quantum-dot phonon energies (see Fig. 5). Therefore, we will be performing transitions from one vibrational eigenstate to another vibrational eigenstate. Such transitions were described in Sec. IV with respect to the ground vibrational state. Consequently, the scheme proposed in this work is not affected by fast phonon dephasing.

Exciton states recombine and thus decay to the ground state by both spontaneous emission of photons and phonons. We denote the recombination lifetime by τ_{re}. Nanocrystals are known to have dark-state recombination times ranging from 10^{-6} s to 10^{-3} s, depending on the material chosen [60,73,91,95]. In our system, τ_{re} will be the fastest decoherence time for individual qubits. One could potentially suppress radiative recombination by placing the whole system in a cavity [107]. Classical calculations of Roukes and co-worker show that nanoscale rods at low temperature have high Q values: $Q \geqslant 10^{10}$ [108]. This implies that the rods are only very weakly coupled to their environments and we can therefore assume that in the quantum regime, the high Q will lead to favorably long decoherence times. Another possible source of decoherence is laser scattering from the support (as opposed to the QDs). The magnitude of scattering is dependent on the difference between the spectra of the quantum dots and the electronic and vibrational modes of the support. A detailed analysis of this potentially important decoherence mechanism is beyond the scope of this paper, due to the many possible materials available for both linear supports and quantum dots. Ideally, one would like to choose a support that has an optical window at the frequencies of the lasers used to perform the qubit operations. Estimations based on the Raman transitions proposed above suggest that this optical window needs to be between 0.1–1 eV and possess a minimal width of 0.1 meV. Conversely, one can take advantage of the optical tunability of the QDs via their size to construct a QD of such size that its transitions are compatible with a specific optical window suggested by the material properties of the support.

B. Parameter space

We now explore for what range of physical parameters quantum computation is possible within our proposed scheme by estimating the two-qubit gate fidelity, $\mathcal{F}$. This fidelity is defined as the trace overlap between the desired and the achieved final state: $\mathcal{F} = \min_{\rho_0} \mathrm{Tr}\, A \rho_0 A^{\dagger} B(\rho_0)$, where A is the exact unitary operator for the gate, B is a superoperator describing the actual evolution of the system that takes the initial density matrix ρ_0 to a final density matrix ρ_f, and ρ_0 ranges over all possible input states. For our two-qubit operations described in Sec. IV B, the fundamental operation is the population transfer to the red sideband, $A = U_1^{n10}$ [Eq. (24)]. B describes both the unitary evolution caused by application of the lasers and the decoherence due to loss of quantum information to the environment. Note that even without decoherence and unknown laser noise, $\mathcal{F}$ can still be less than unity due to deviations from the approximations used to derive A. Most importantly, deviations from the rotating-wave approximation can lead to unwanted population in spectator states.

The resulting value of $\mathcal{F}$ is determined by two constraints: the decoherence time of the system and the spectral resolution of the gate. As a result of the use of the phonon bus in the two-qubit gate construction, both this proposal and the ion-trap proposal [7,10] have gate times that are dependent on the number of qubits. Therefore the quantity of interest is

the fidelity of a sideband operation on an array of N quantum dots. First, we note that $\mathcal{F}$ is limited by the recombination time of the qubit states, $\tau_{re} = 1/\Gamma$. Naturally, the recombination time τ_{re} must be larger than the sideband operation time, $\tau_A = \pi/(2\Omega_2)$, if the operation is to be successful. One can then define an upper limit on the fidelity that takes into account the statistically independent recombination of the exciton states of all N quantum dots. This background fidelity assumes that τ_{re} is the same for all N quantum dots and it does not account for errors deriving from the interactions with the driving laser field. The background fidelity is then

$$\mathcal{F} \approx 1 - \frac{\tau_A}{\tau_{re}} = 1 - \frac{\pi N \Gamma}{2\Omega_2}. \qquad (34)$$

$\mathcal{F}$ is also limited by the spectral resolution. We assume that the difference in frequency between the lasers is tuned to be resonant with the energy difference between the two states of interest, Fig. 4. The energy difference between the states includes the relative ac Stark shift induced by the lasers. Omitting the adjustment of the laser frequency for the ac Stark shift will lead to gates of reduced fidelity [110,111]. The primary concern is that the phonon modes should be spectrally resolvable. As described in Sec. II, the use of nodal and antinodal lasers allows us to transfer population to the vibrational sideband and at the same time forbid population transfer to the carrier, i.e., to the excitonic states of the QD. This constrains the operation frequency Ω_2 to be smaller than the separation between phonon modes, $\Delta\omega = \omega_{m+1}^s - \omega_m^s$. For small m, and for $\Delta\omega \approx \omega_1^s$, we can then write this constraint as

$$\Omega_2 < \omega_1^s. \qquad (35)$$

The population transfer to the off-resonant state will be of the order of $4g^2/[4g^2 + (\delta)^2]$, the result for a two-level system interacting with a periodic perturbation of strength g that is off-resonant by a frequency difference δ [98]. In our case, $g = \Omega_2$ and $\delta = \Delta\omega \approx \omega_1^s$. However, numerical calculations [110] have shown that the population transfer to the off-resonant state for an ion-trap system is more accurately estimated by $2g^2/[4g^2 + (\delta)^2]$. Note that in Ref. [110] $g = \Omega/2$, the coupling to the carrier transition, and $\delta = \omega_z$, the ion-trap mode vibrational frequency. The advantage of the standing-wave laser configuration is now apparent. For the traveling-wave laser configuration, the population transfer to the off-resonant state is $2(\Omega_2/\eta)^2/[4(\Omega_2/\eta)^2 + (\omega_1^s)^2]$ $\approx 2(\Omega_2/\eta\omega_1^s)^2$ [or, in the notation of Ref. [110], $\frac{1}{2}(\Omega/\omega_z)^2$]. However, in the standing-wave configuration, one finds that the population transfer is $2(\Omega_2)^2/[4(\Omega_2)^2 + (\omega_1^s)^2] \approx 2(\Omega_2/\omega_1^s)^2$. Since $\eta \ll 1$ the off-resonant population transfer is significantly reduced when one uses the standing-wave configuration. We can now write down a fidelity that takes into account both the background fidelity, Eq. (34), and the population loss to the most significant spectator state. The fidelity per sideband operation A is then

$$\mathcal{F} \approx 1 - \frac{\pi N \Gamma}{2\Omega_2} - 2\left(\frac{\Omega_2}{\omega_1^s}\right)^2 \tag{36}$$

in the standing-wave configuration. We emphasize again that if the laser fields are used in a traveling-wave configuration, the fidelity is significantly decreased due to transitions to the carrier state, resulting in $\mathcal{F} \simeq 1 - \pi N \Gamma / 2\Omega_2 - 4(\Omega_2 / \eta \omega_1^s)^2$.

One can now maximize the fidelity with respect to the coupling strength Ω_2 for a sideband operation made on an N-qubit array. Since

$$\Omega_2^{\mathcal{F}\max} = \left[\frac{\pi(\omega_1^s)^2 N \Gamma}{8}\right]^{1/3}, \tag{37}$$

for given Γ and ω_1^s, the maximum fidelity can be written as

$$\mathcal{F}_{\max} = 1 - 3\left(\frac{\pi N \Gamma}{2\sqrt{2}\,\omega_1^s}\right)^{2/3}. \tag{38}$$

Evaluation of the optimal operation frequency depends then only on the factors in Eq. (37). Inspection of the contributions to Ω_2 [Eq. (27)] shows that the underlying adjustable parameters controlling the fidelity, in general, Eq. (36), are the intensities I_1, I_2, the detuning Δ, and the Lamb-Dicke parameter η. However, the schematic shown in Fig. 4 shows that there are some additional constraints. Thus, it is essential that the inequality $\omega_1^s < \Delta < \omega_1^d$ be satisfied in order to avoid

unwanted coupling to both the internal phonons and the linear-support phonons. In addition, we require that both $|\Omega_{\mathbf{k}_1}^{ji}|$ and $\eta_{01\mathbf{k}_2}|\Omega_{\mathbf{k}_2}^{fj}|$ are smaller than Δ, in order to avoid populating the intermediate level, $|\Psi_j\rangle$. Hence, the internal phonon energies define an energy scale, which also constrains our system (see Fig. 5).

Furthermore, combining Eqs. (20), (27), and (37), one finds that

$$|\Omega_{\mathbf{k}_1}^{ji}\,\eta_{01\mathbf{k}_2}\Omega_{\mathbf{k}_2}^{fj}| = \Delta\left[\frac{\pi(\omega_1^s)^2 N \Gamma}{8}\right]^{1/3}. \tag{39}$$

Analysis of three level systems has shown that in order to maximize Raman population transfer between states $|\Psi_i\rangle$ and $|\Psi_f\rangle$, the coupling strength between $|\Psi_i\rangle$ and $|\Psi_j\rangle$ and $|\Psi_f\rangle$ and $|\Psi_j\rangle$ should be equal [99]. In the atomic case this usually implies that the respective Rabi frequencies between electronic states, $|\Omega_{\mathbf{k}_1}^{ji}|$ and $|\Omega_{\mathbf{k}_2}^{fj}|$, are equal. However, in our case, with the use of nodal and antinodal lasers and coupling to the support phonons, the equivalent condition is that

$$|\Omega_{\mathbf{k}_1}^{ji}| = \eta_{01\mathbf{k}_2}|\Omega_{\mathbf{k}_2}^{fj}|. \tag{40}$$

Therefore, manipulation of Eqs. (19), (39), and (40) allows us to determine the intensity values, I_1 and I_2, necessary for maximum-fidelity operations,

$$I_1 = \frac{\hbar\Delta}{2\pi\alpha}\left[\frac{\pi(\omega_1^s)^2 N \Gamma}{8}\right]^{1/3} \frac{1}{\left|\langle\Psi_j|\boldsymbol{\epsilon}_1\cdot(\mathbf{r}_e - \mathbf{r}_h)|\Psi_i\rangle\prod_l F_{00l}^{ji}\right|^2}, \tag{41}$$

$$I_2 = \frac{\hbar\Delta}{2\pi\alpha}\left[\frac{\pi(\omega_1^s)^2 N \Gamma}{8}\right]^{1/3}\frac{1}{\eta_{01\mathbf{k}_2}^2}\frac{1}{\left|\langle\Psi_f|\boldsymbol{\epsilon}_2\cdot(\mathbf{r}_e - \mathbf{r}_h)|\Psi_j\rangle\prod_l F_{00l}^{fj}\right|^2}$$

$$= \frac{\Delta\lambda L}{2\pi\alpha}\left[\frac{\pi(\omega_1^s)^5 N \Gamma}{8}\right]^{1/3}\frac{1}{|\mathbf{k}_2|^2}\frac{1}{\left|\langle\Psi_f|\boldsymbol{\epsilon}_2\cdot(\mathbf{r}_e - \mathbf{r}_h)|\Psi_j\rangle\prod_l F_{00l}^{fj}\right|^2}. \tag{42}$$

Equations (38), (41), and (42) summarize the limits to implementation of this quantum-dot–quantum-linear-support scheme. To maximize the fidelity we need to increase the frequency of the phonon bus, ω_1^s. However, as this frequency increases, the increased intensity necessary to reach the maximum fidelity will lead to unwanted evolutions not considered in our simple fidelity equation, Eq. (38). These unwanted evolutions include quadrupolar excitation to higher electronic states. Such transitions will not be removed by the use of nodal and antinodal lasers [9]. Consequently, it is useful to define maximal laser intensities, $I_1^{\max}$ and $I_2^{\max}$, such that Eq. (38) is valid for $I_1 < I_1^{\max}$ and $I_2 < I_2^{\max}$. There-

fore the magnitude of ω_1^s is restricted and thereby imposes a constraint on the phonon spectrum of the linear support. Furthermore, scalability is also limited by the additional unwanted evolutions, since the required intensity to achieve maximum fidelity also increases with N.

There are also physical constraints on the density and length of the support. We choose a minimal density $\lambda_0 = 10$ amu/Å^{-1} that corresponds approximately to a chain of pure carbon atoms with bond length 1.5 Å. The length of the support, L, is determined by the number of QDs, N, and by the spatial width of the laser, l. Thus for identical dots, we have $L = lN$. One could use QDs having no spectral overlap,

obtained by making the dots of sufficiently different sizes, in order to achieve more qubits per unit length.

Notice that when one rewrites L in terms of N that the intensity of the nodal laser, I_2, has a stronger N dependence than the intensity of the antinodal laser, I_1. Physically, this is due to the increased inertia of the system and is quantified by the Lamb-Dicke parameter η. From Eq. (5) and Sec. (III B), $\eta \propto M^{-1/2}$, where M is the total mass of the support, $M = \lambda L$, so that $I_2 \propto M$ [Eq. (42)]. This coupled with our expression for the maximal gate fidelity, Eq. (38), yields $I_2 \propto N^{4/3}$. Note that we have used the Lamb-Dicke parameter consistent with the definition made in Ref. [110], which has an inverse N dependence.

To determine the scalability of our system, we examine the maximum number of QDs that can be sustained by a support having given values of ω_1^s and $\lambda/\lambda_{\min}$, and provide an acceptable level of fidelity for the sideband operation, $A = U_1^{n10}$. We do this by requiring the following three constraints to be simultaneously satisfied: (i) $\mathcal{F} = \mathcal{F}_{\max}$, (ii) $I_2 \leqslant I_2^{\max}$, and (iii) $\mathcal{F}_{\max} > 1 - \varepsilon$, where ε can be thought of as the error rate per gate frequency. The first condition states that maximum gate fidelity, Eq. (38), is achieved given the support and quantum-dot parameters, ω_1^s and Γ, respectively. The second condition states that the laser frequency I_2 should not exceed the maximum allowed value (see above). Equation (42) together with the considerations in the previous paragraph shows that I_2 is dependent on the number of quantum dots N. For the range of parameters considered here, I_1 is always smaller that $I_1^{\max}$. Hence the maximum number of qubits will be determined by the intensity threshold of the system at a node of the laser field. The third condition ensures that one is able to perform an operation with success greater than a certain threshold value (equal to $1 - \varepsilon$). Combining these inequalities leads to limits on the number of qubits for a given system. Conditions (i) and (iii) can be manipulated to yield the following constraint on N:

$$N \leqslant \omega_1^s \left(\frac{2\varepsilon}{3} \right)^{3/2} \frac{1}{\pi \Gamma}. \quad (43)$$

On the other hand, conditions (i) and (ii) yield a constraint with an inverse power dependence on ω_1^s. One finds that

$$N \leqslant (\omega_1^s)^{-5/4} (I_2^{\max})^{3/4} \left(\frac{8}{\pi \Gamma} \right)^{1/4} \left(\frac{2\pi \alpha}{\Delta \lambda l} |\mathbf{k}_2|^2 \right.$$

$$\times \left. \langle \Psi_f | \boldsymbol{\epsilon}_2 \cdot (\mathbf{r}_e - \mathbf{r}_h) | \Psi_j \rangle \prod_l F_{00l}^{fj} \right|^2 \right)^{3/4}. \quad (44)$$

One can then analyze $N_{\max}$, the maximum allowed value of N, as a function of the linear-support frequency ω_1^s. The combination of Eqs. (43) and (44) results in a cusped function for $N_{\max}$ and is discussed in detail in Sec. VI for both a direct-band-gap semiconductor (CdTe) and an indirect-band-gap semiconductor (Si).

The above discussion has focused on the fidelity for a single-component operation, $A = U_1^{n10}$, of the C-phase gate, $U_{C\text{-phase}} \equiv U_1^{n10} U_2^{n'20} U_1^{n10}$. We have termed this a sideband

operation fidelity. Similar arguments may be made to derive the full C-phase gate fidelity, resulting in the expression

$$\mathcal{F}_{C\text{-phase}} \approx 1 - \frac{2\pi N \Gamma}{\Omega_2} - 4 \left(\frac{\Omega_2}{\omega_1^s} \right)^2. \quad (45)$$

This is lower than the sideband operation fidelity, both because of the effect of multiple couplings to spectator states and because of an increased operation duration ($\tau_{C\text{-phase}} = 4\tau_A$). In the presentation of numerical results in the next section we shall refer only to the prototypical sideband operation fidelity, $\mathcal{F}$ of Eq. (36).

VI. NUMERICAL ESTIMATES FOR SPECIFIC NANOCRYSTAL SYSTEMS

A. CdTe

CdTe nanocrystals are an example of direct-band-gap cubic crystal semiconductor QDs. Using parameters found in Ref. [112], we have performed the calculations summarized in the previous sections, using previous results of Efros *et al.* [60] and Takagahara [100] for the EMA analysis. Although the dark states have infinite lifetimes in the EMA approximation, both experimental [113] and tight-binding calculations for the analogous CdSe system [73] yield radiative recombination rates $\Gamma \sim 10^6$ Hz.

We analyze here nanocrystals with $R = 20$ Å. For this size, the frequency of the lowest internal phonon is $\omega_1^d = 2.45 \times 10^{12}$ Hz. Assuming a minimal separation of a single order of magnitude between the energy spacings ω^d and Δ, we set $\Delta = 10^{11}$ Hz. The energy separation between the $1S_{1/2}1S_{3/2}$ and $1S_{1/2}1P_{5/2}$ multiplets is ~ 0.4 eV in the EMA, which leads to required wave vectors $k_1 \simeq k_2 \simeq 2.1$ μm^{-1} for the irradiating lasers in the two-qubit gates. For the specific CdTe states introduced above (Sec. III A), we calculate the dipole moments to be $\langle \Psi_{-1}^{aux}(\mathbf{r}_e, \mathbf{r}_h) | \boldsymbol{\epsilon}_2 \cdot \mathbf{r} | 0 \rangle = 0.11R$, $\langle \Psi_{-1}^{aux}(\mathbf{r}_e, \mathbf{r}_h) | \boldsymbol{\epsilon}_1 \cdot \mathbf{r} | 1 \rangle = -0.013R$, where $\boldsymbol{\epsilon}_2 = (1/\sqrt{2})(\hat{x} + i\hat{y})$ and $\boldsymbol{\epsilon}_1 = (1/\sqrt{2})(\hat{x} - i\hat{y})$. Furthermore, we have calculated the Frank-Condon overlap to be $\Pi_l F_{00l}^{aux0} = 0.98$ and $\Pi_l F_{00l}^{aux1} = 0.98$. We assume that the spatial width of our lasers is diffraction limited. A reasonable estimate of this width is then $l = 3\mu m$. At constant frequency, an increase in the number of qubits requires an increase in the laser intensity in order to maintain maximum-fidelity operations. We estimate that $I_2^{\max} = 10^{12}$ W/cm^2 is the intensity at which the nonresonant quadrupole interactions begin to rise in CdTe quantum dots. However, the intensity could potentially have stricter limitations depending on the spectra of the specific support chosen. As mentioned above for the range of parameters we have examined, the intensity of the antinodal laser is weak enough so as not to lead to unwanted time evolutions.

In Fig. 6, $N_{\max}$ is plotted as a function of ω_1^s for two linear-support densities and for a modest threshold of one error for every ten operations ($\varepsilon = 0.1$). At low frequencies, Eq. (43) limits $N_{\max}$ and increasing the values of ω_1^s leads to larger values of N for a fixed $\mathcal{F}_{\max}$. In contrast, higher fre-
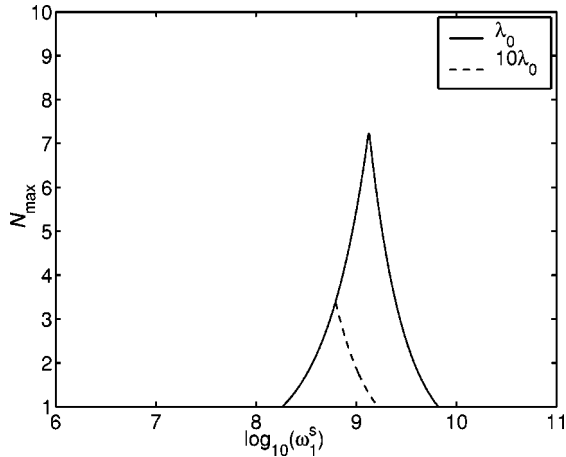
FIG. 6. Dependence of the maximum number of 20-Å CdTe nanocrystal quantum-dot qubits for which quantum computation is sustainable, subject to the three conditions determined by analysis of the two-qubit gate (see text): (i) the fidelity per gate, $\mathcal{F} = \mathcal{F}_{max}$; (ii) the antinodal laser intensity, $I_2 \leqslant I_2^{\max}$; and (iii) $\mathcal{F}_{max} > 1 - \varepsilon$, where ε can be thought of as the error rate per gate frequency. The figure shows a plot of N_{max} as a function of the frequency of the linear-support phonon mode, ω_1^s, for two values of the linear support densities, $\lambda_0 = 10$ amu/Å, $\lambda = 10\lambda_0$, and $\varepsilon = 0.1$. The extremum of the functions corresponds to the maximum possible scalability achievable for 20-Å CdTe nanocrystal qubits. For larger values of ω_1^s, the larger values of $\mathcal{F}^{max}$ that are possible, in principle, are offset by the need for higher-intensity lasers. In this situation it is possible to support more qubits than are shown here by relaxing the first constraint. However, one thereby loses the advantage of the increase in $\mathcal{F}_{max}$ as ω_1^s is increased.

quencies require stronger laser intensities [Eq. (42)] so that eventually the limits on the intensity given in condition (ii) begin to reduce the maximum possible number of quantum dots, leading to the turnover in Fig. 6. Figure 6 also shows that the optimal value of N_{max}, which we denote by N_c, is reduced for larger support densities. In Fig. 7, we now plot N_c as a function of the error threshold ε, for a range of linear densities λ. We see that even for two-qubit quantum devices
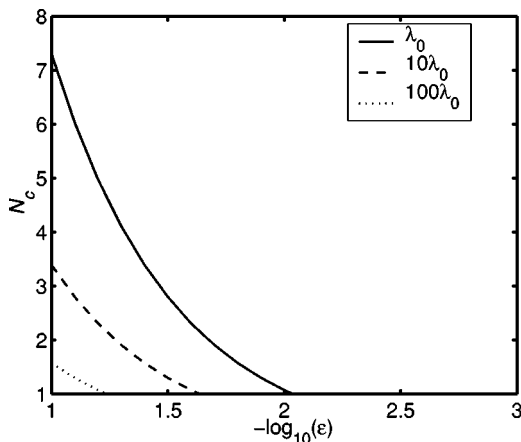

FIG. 7. Dependence of the optimal number of CdTe nanocrystals, N_c (peaks in Fig. 6) on the error threshold ϵ plotted for various linear-support densities. $\lambda_0 = 10$ amu/Å.

one must allow $\varepsilon > 0.02$, or approximately one error for every 50 operations. Even at the modest threshold value, $\varepsilon = 0.1$, one can only support seven qubits. Clearly, CdTe excitons are thus not good candidates for scalable qubits within this scheme. The underlying reason is that the recombination time of the dark states, while longer than the operation time, is not sufficiently long to provide high-fidelity operations.

B. Si

Si and other indirect-band-gap bulk materials exhibit longer exciton-recombination lifetimes than direct-band-gap materials such as CdTe. Although EMA descriptions of Si nanocrystals exist, many subtleties are required to obtain accurate excitonic states [62]. These have also been calculated in semiempirical tight-binding approaches [95], as well as via pseudopotential methods [77]. The advantage of tight-binding descriptions is that the optical properties of the nanocrystal can be determined with inclusion of realistic surface effects [114]. We estimate the feasibility of using Si nanocrystals here using the detailed Si excitonic band structure previously calculated within a semiempirical description [95]. In order to suppress phonon emission we choose states that correspond to either the exciton ground state, or lie within the minimal phonon energy of the exciton ground state. The minimal phonon energies ω_0^d are taken from EMA calculations made by Takagahara [100], and are approximately equal to 5 meV for a nanocrystal of 20 Å radius. One disadvantage of the tight-binding description is that the states are no longer describable as states with well-defined angular momentum, and the calculation of electron-phonon coupling is not straightforward. Therefore, we employ the EMA analysis of Takagahara for this. The Franck-Condon factors are estimated to be ~0.9 between electronic states derived from the same multiplet. Calculations and experiments on Si reveal dark states with recombination times of microseconds [95]. Tight-binding states lack well-defined quantum numbers. However, for spherical dots of 20 Å there are multiple dark states that satisfy our phonon-emission criteria [95]. States from these multiplets can be used to form our logic and auxiliary states. Calculated Raman transitions between these states have quantitatively similar values to those obtained for CdTe above.

Given an assumed radiative-recombination rate $\Gamma = 10^3$ Hz [95], we perform an analysis similar to the one above for CdTe. In Fig. 8 N_{max} is plotted as a function of ω_1^s for a variety of densities λ and a threshold of one error every 10 gates ($\varepsilon = 0.1$). Fig. 8 implies that one could construct a quantum computer composed of 700 quantum dots if $\varepsilon = 0.1$. In Fig. 9, the extremum value of N_{max}, N_c is plotted as a function of ε for a range of λ values. The results are also summarized in Table I. One sees that, unlike CdTe, for Si there now exists the possibility of building a quantum processor that possesses an appreciably lower error rate of ~1 error every thousand gates. Most encouragingly, it seems possible to construct a small quantum-information processor (5–10 qubits) with a larger linear-support density $10\lambda_0$ and an error rate of $\varepsilon \leqslant 10^{-3}$. Naturally, from an experimental perspective it would probably be more realistic to use a sup-
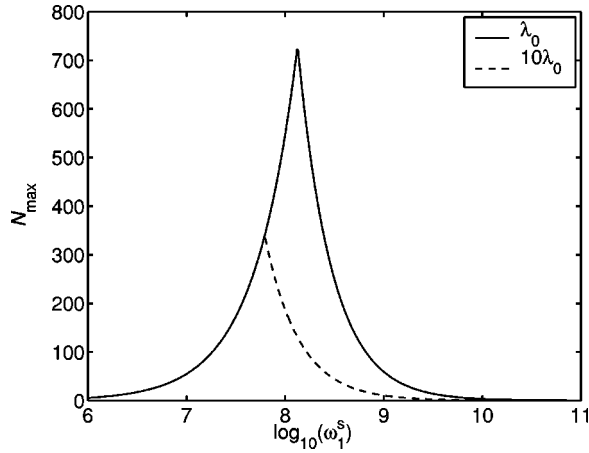
FIG. 8. Dependence of the maximum number of 20-Å Si nanocrystal quantum-dot qubits for which quantum computation is sustainable, subject to the three conditions determined by analysis of the two-qubit gate (see text): (i) the fidelity per gate, $\mathcal{F}=\mathcal{F}_{\max}$; (ii) the antinodal laser intensity, $I_2 \leqslant I_2^{\max}$, and (iii) $\mathcal{F}_{\max} > 1-\varepsilon$, where ε can be thought of as the error rate per gate frequency. The figure shows a plot of $N_{\max}$ as a function of the frequency of the linear-support phonon mode, ω_1^s, for two values of the linear support densities, $\lambda_{\min}=10$ amu/Å and $\lambda=10\lambda_{\min}$ and $\varepsilon=0.1$. The extremum of the functions corresponds to the maximum possible scalability achievable for 20-Å Si nanocrystal qubits. The degree of scalability is greater for the indirect band-gap material than for the direct-band-gap CdTe nanocrystals shown in Fig. 6, and shows less dependence on the linear-support density λ.

port having a density at least ten times greater than our proposed minimal density λ_0 that was estimated for a pure carbon chain (e.g., DNA [45], carbon nanotubes, etched supports, etc.).

VII. CONCLUSIONS

We have developed a condensed-phase scheme for a quantum computer that is analogous to the gas-phase ion-
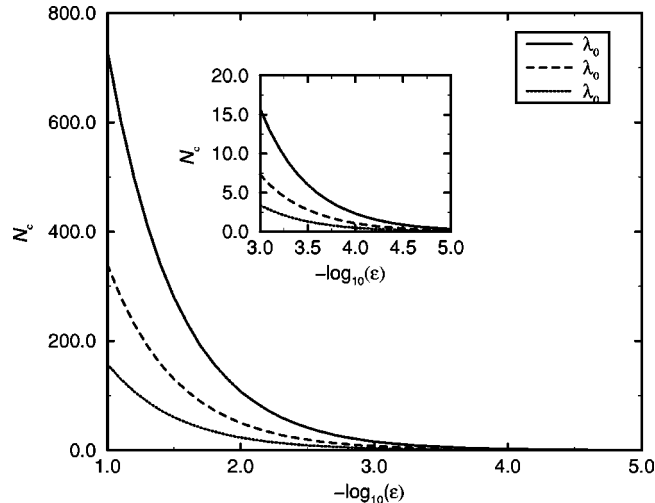

FIG. 9. Dependence of the optimal number of Si nanocrystals, N_c (peaks in Fig. 8) on the error threshold ϵ plotted for various linear-support densities. $\lambda_0=10$ amu/Å.

TABLE I. For a given error threshold ε and support density λ, the table shows the optimal value of $N_{\max}$, N_c for CdTe and Si nanocrystals. $\lambda_0=10$ amu/Å .

$-\log_{10}(\varepsilon)$	λ/λ_0	N_c (CdTe)	N_c (Si)
1	1	7	731
	10	3	339
	100	1	158
2	1	1	107
	10	0	50
	100	0	23
3	1	0	16
	10	0	7

trap proposal and have explored the feasibility of implementing this scheme with semiconductor quantum dots coupled by a quantum linear support consisting of a string or rod. We have found that the Cirac-Zoller scheme of qubits coupled by a quantum-phonon-information bus is also applicable in the solid state, and that there exist some advantages to a condensed-phase implementation. One such advantage is that there is a potential for significantly less noise in the information bus than in the corresponding gas-phase scheme. Calculations by Roukes and co-worker [108] suggest that much higher Q factors may be found for nanorods than are currently obtainable in ion traps. Clearly the extent of the usefulness of our proposal will be very dependent on the choice of materials. To that end we have analyzed the fidelity for two-qubit operations for several candidate systems, including both direct- and indirect-gap semiconductor quantum dots. We have presented the results of numerical calculations for implementation of the scheme with CdTe and Si quantum dots, coupled via either quantum strings or rods. While neither of these prototypical direct- and indirect-band-gap materials reach the level of fidelity and size required for large-scale quantum computation, the indirect-gap quantum dots (Si) do show a reasonably high fidelity with an array of a few tens of dots.

One very revealing result of these explicit calculations of fidelity for one- and two-qubit gates is the limited scalability. The scheme initially appears highly scalable in concept due to the solid-state-based architecture. However, the detailed analysis given here showed that the dependence of the Lamb-Dicke parameter η on the mass of the support is a basic problem that essentially limits the scalability to a few tens of qubits even in the more favorable indirect-gap materials. The main drawback of this condensed-phase scheme over the ion-trap scheme is therefore the large reduction in η deriving from the introduction of massive supports. Such a reduction has two important consequences. First, the laser intensities need to be increasingly large to perform operations faster than the decoherence time. Second, such large laser intensities necessitate the use of nodal and antinodal lasers [9,110]. Without these features, the probability of gate error is extremely high due to transitions to the carrier. This means that several of the alternative schemes proposed for ion-trap computation [10,111] would not provide feasible condensed-phase analogs [although the recent scheme of

Childs and Chuang [92], which allows computation with two-level ions (or quantum dots) by using both the blue and red sidebands could also be feasible in the condensed phase].

Additional sources of decoherence that have been neglected here (scattering off the support, vibrational and electronic transitions in the support) will also act to limit the number of operations. However, one source of decoherence that can be eliminated or at least reduced is dephasing from the coupling to phonon modes of the support. This is a consequence of the requirement of extremely narrow bandwidth lasers, and therefore implies that a similar lack of dephasing will hold for other optical experiments on quantum dots that use narrow bandwidths. One such example is the proposal to couple quantum dots via whispering-gallery modes of glass microspheres [23]. More generally, this result offers a route to avoid dephasing for other spectral measurements on quantum dots [115].

An interesting additional application for this proposal is the laser cooling of nanorods. A single QD could be placed or even etched on a nanostructure. A laser tuned to the red support phonon sideband of a QD-excited electronic state would excite the energy of the nanocrystal, and at the same time lower the average phonon occupation of the support. When the unstable state relaxes, the most probable transition is the carrier transition. The net result is that the emitted phonon is blueshifted compared to the excitation pulse. The extra energy carried away by the emitted photon is thereby removed from the motional energy of the QD.

The essential physical problem encountered in this condensed-phase realization of the qubits coupled by phonon modes is the recombination lifetime of the qubit states, i.e., the exciton radiative lifetime. In principle, this could be ameliorated by using hyperfine states of a doped nanocrystal. Recent experimental results demonstrating electronic doping of semiconductor quantum dots offer a potential route to controlled access of these states [116]. The feasibility study presented in this paper does indicate that although the detailed physics of the qubits and their coupling is considerably more complicated in the condensed phase than in the gas phase, limited quantum computation may be possible with phonon-coupled solid-state qubits. Further analysis and development of suitable nanoscale architectures and materials is therefore warranted.

APPENDIX: COORDINATE REPRESENTATION OF ELECTRON AND HOLE STATES

We give here the coordinate representation of the electron and hole states. These states were derived in [60] [We em-

ploy a slightly different phase convention. Efros *et al.* when calculating the exchange Hamiltonian, $\gamma \vec{S}_h \cdot \vec{S}_e$, between the hole and electron spin, $\vec{S}_h$ and $\vec{S}_e$, use the convention, $\vec{S}_h \cdot \vec{S}_e = S_h^z S_e^z + i/2(S_h^+ S_e^- - S_h^- S_e^+)$. We instead use the convention that $\vec{S}_h \cdot \vec{S}_e = S_h^z S_e^z + \frac{1}{2}(S_h^+ S_e^- + S_h^- S_e^+)$]. For convenience, we repeat the definitions of our qubit states [Eq. (9)] in slightly more detailed notation,

$$|0\rangle = |\Psi_{1/2,1/2}^S(\mathbf{r}_e)\rangle|\Psi_{3/2,3/2}^S(\mathbf{r}_h)\rangle,$$

$$|1\rangle = |\Psi_{1/2,-1/2}^S(\mathbf{r}_e)\rangle|\Psi_{3/2,-3/2}^S(\mathbf{r}_h)\rangle,$$

$$|2\rangle = \frac{1}{\sqrt{2}}[|\Psi_{1/2,-1/2}^S(\mathbf{r}_e)\rangle|\Psi_{3/2,1/2}^S(\mathbf{r}_h)\rangle$$
$$- |\Psi_{1/2,1/2}^S(\mathbf{r}_e)\rangle|\Psi_{3/2,-1/2}^S(\mathbf{r}_h)\rangle].$$

The electron states are simply the solutions to a free spin-1/2 particle in a spherical hard-wall box,

$$|\vec{S}_e\rangle \equiv |\Psi_{1/2,\pm 1/2}^S(\mathbf{r})\rangle = \sqrt{\frac{2}{R}} \frac{\sin(\pi r/R)}{r} Y_0^0(\theta,\varphi)\left|S,\pm\frac{1}{2}\right\rangle,$$
$$(A1)$$

where R is the radius of the dot and Y_l^m are spherical harmonics. S is a conduction-band Bloch function and $\pm\frac{1}{2}$ is the z projection of the electron spin,

$$\left|S,\pm\frac{1}{2}\right\rangle = |L=0,m_L=0\rangle\left|m_s=\pm\frac{1}{2}\right\rangle. \quad (A2)$$

The holes states can be written explicitly as

$$|\Psi_{3/2,\pm 1/2}^S(\mathbf{r})\rangle = -R_0(r)Y_0^0|u_{\pm 1/2}\rangle - R_2(r)\left(\sqrt{\frac{2}{5}}Y_2^{\pm 2}|u_{\mp 3/2}\rangle\right.$$
$$+ \sqrt{\frac{2}{5}}Y_2^{\mp 1}|u_{\pm 3/2}\rangle - \sqrt{\frac{1}{5}}Y_2^0|u_{\pm 1/2}\rangle\right)$$
$$\times |\Psi_{3/2,\pm 3/2}^S(\mathbf{r})\rangle$$
$$= -R_0(r)Y_0^0|u_{\pm 3/2}\rangle - R_2(r)\left(\sqrt{\frac{2}{5}}Y_2^{\pm 2}|u_{\mp 1/2}\rangle\right.$$
$$- \sqrt{\frac{2}{5}}Y_2^{\pm 1}|u_{\pm 1/2}\rangle + \sqrt{\frac{1}{5}}Y_2^0|u_{\pm 3/2}\rangle\right),$$

where R_l are the envelope functions and $|u_{m_J}\rangle$ are the valence-band Bloch functions.

The radial functions are

$$R_2(r) = \frac{A}{R^{3/2}}\left[j_2(\phi r/R) + \frac{j_0(\phi)}{j_0(\phi\sqrt{\beta})}j_2(\phi\sqrt{\beta}r/R)\right],$$

$$R_0(r) = \frac{A}{R^{3/2}}\left[j_0(\phi r/R) - \frac{j_0(\phi)}{j_0(\phi\sqrt{\beta})}j_0(\phi\sqrt{\beta}r/R)\right],$$

where j_l are spherical Bessel functions, $\beta = m_{lh}/m_{hh}$ is the ratio of the light to heavy hole masses, and ϕ is the first root of the equation

$$j_0(\phi)j_2(\sqrt{\beta}\phi) + j_2(\phi)j_0(\sqrt{\beta}\phi) = 0.$$

The constant A is defined by the normalization condition

$$\int_0^R [R_0^2(r) + R_2^2(r)]r^2 dr = 1.$$

The valence-band Bloch functions are given by

$$|u_{\pm 3/2}\rangle = |L=1, m_L = \pm 1\rangle |m_s = \pm 1/2\rangle,$$

$$|u_{\pm 1/2}\rangle = \frac{1}{\sqrt{3}}[\sqrt{2}|L=1, m_L=0\rangle|m_s=\pm 1/2\rangle$$

$$+ |L=1, m_L=\pm 1\rangle|m_s=\mp 1/2\rangle].$$

For our Raman-transition scheme, we have used states that were not analyzed in [60]. In particular, these states are from the $1S_e 1P_{5/2}$ exciton multiplet. To find these we used techniques developed in [117], and then calculated the eigenstates of the exchange coupling using the method of [60]. A Raman transition connects states of equal parity through a state of opposite parity. Therefore, the states of interest to us are the $F_z = \pm 1$ states,

$$|\Psi_{\pm 1}^v\rangle = -\frac{1}{\sqrt{3}}[|\Psi_{1/2,\mp|1/2}^S(\mathbf{r}_e)\rangle|\Psi_{5/2,\pm 3/2}^P(\mathbf{r}_h)\rangle$$

$$+ \sqrt{2}|\Psi_{1/2,\pm 1/2}^S(\mathbf{r}_e)\rangle|\Psi_{5/2,\pm 1/2}^P(\mathbf{r}_h)\rangle].$$

The electron state is as above. The hole state can be written explicitly as

$$|\Psi_{5/2,\pm 3/2}^P(\mathbf{r})\rangle = R_1(r)\left(\sqrt{\frac{2}{5}}Y_1^0|u_{\pm 3/2}\rangle + \sqrt{\frac{3}{5}}Y_1^{\pm 1}|u_{\pm 1/2}\rangle\right)$$

$$+ R_3(r)\left(3\sqrt{\frac{1}{35}}Y_3^0|u_{3\pm/2}\rangle\right.$$

$$\left. - \frac{1}{2}\sqrt{\frac{7}{5}}Y_3^{\pm 1}|u_{\pm 1/2}\rangle + \sqrt{\frac{1}{14}}Y_3^{\pm 2}|u_{\mp 1/2}\rangle\right.$$

$$\left. + \frac{3}{2}\sqrt{\frac{1}{7}}Y_3^{\pm 3}|u_{\mp 3/2}\rangle\right),$$

$$|\Psi_{5/2,\pm 1/2}^P(\mathbf{r})\rangle = R_1(r)\left(\sqrt{\frac{1}{10}}Y_1^{\mp 1}|u_{\pm 3/2}\rangle \sqrt{\frac{3}{5}}Y_1^0|u_{\pm 1/2}\rangle\right.$$

$$\left. + \sqrt{\frac{3}{10}}Y_1^{\pm 1}|u_{\mp 1/2}\rangle\right) + R_3(r)$$

$$\times \left(3\sqrt{\frac{3}{70}}Y_3^{\mp 1}|u_{\pm 3/2}\rangle - \sqrt{\frac{6}{35}}Y_3^0|u_{\pm 1/2}\rangle\right.$$

$$\left. - \sqrt{\frac{1}{70}}Y_3^{\pm 1}|u_{\mp 1/2}\rangle + \sqrt{\frac{3}{7}}Y_3^{\pm 2}|u_{\mp 3/2}\rangle\right),$$

where R_l are the envelope functions and $|u_{m_J}\rangle$ are the valence-band Bloch functions given above.

The radial functions are

$$R_3(r) = \frac{B}{R^{3/2}}\left[j_3(\phi' r/R) + \frac{2j_1(\phi')}{3j_1(\phi'\sqrt{\beta})}j_3(\phi'\sqrt{\beta}r/R)\right],$$

$$R_1(r) = \frac{B}{R^{3/2}}\left[j_1(\phi' r/R) - \frac{j_1(\phi')}{j_1(\phi'\sqrt{\beta})}j_1(\phi'\sqrt{\beta}r/R)\right],$$

where ϕ' is the first root of the equation

$$j_1(\phi)j_3(\sqrt{\beta}\phi) + \frac{2}{3}j_1(\phi)j_3(\sqrt{\beta}\phi) = 0 \qquad \text{(A3)}$$

and B is defined by the normalization condition

$$\int_0^R [R_1^2(r) + R_3^2(r)]r^2 dr = 1. \qquad \text{(A4)}$$

[1] P.W. Shor, SIAM J. Comput. **26**, 1484 (1997).

[2] L.K. Grover, Phys. Rev. Lett. **79**, 325 (1997).

[3] D.G. Cory, A.F. Fahmy, and T.F. Havel, Proc. Natl. Acad. Sci. USA **94**, 1634 (1997).

[4] N. Gershenfeld and I.L. Chuang, Science **275**, 350 (1997).

[5] D.G. Cory, R. Laflamme, E. Knill, L. Viola, T.F. Havel, N. Boulant, G. Boutis, E. Fortunato, S. Lloyd, R. Martinez, C. Negrevergne, M. Pravia, Y. Sharf, G. Teklemariam, Y.S. Weinstein, and W.H. Zurek, Fortschr. Phys. **48**, 875 (2000).

[6] F. Yamaguchi and Y. Yamamoto, Appl. Phys. A: Mater. Sci. Process. **68**, 1 (1999).

[7] J.I. Cirac and P. Zoller, Phys. Rev. Lett. **74**, 4091 (1995).

[8] D.J. Wineland, C. Monroe, W.M. Itano, D. Leibfried, B.E. King, and D.M. Meekhof, J. Res. Natl. Inst. Stand. Technol. **103**, 259 (1998), http://nvl.nist.gov/pub/nistpubs/jres/103/3/cnt103-3.htm.

[9] D.F.V. James, Appl. Phys. B: Lasers Opt. **66**, 181 (1998).

[10] A. Sorensen and K. Molmer, Phys. Rev. Lett. **82**, 1971 (1999).

[11] Q.A. Turchette, C.J. Hood, W. Lange, H. Mabuchi, and H.J.

Kimble, Phys. Rev. Lett. **75**, 4710 (1995).

[12] G.K. Brennen, C.M. Caves, P.S. Jessen, and I.H. Deutsch, Phys. Rev. Lett. **82**, 1060 (1999).

[13] M. Woldeyohannes and S. John, Phys. Rev. A **60**, 5046 (1999).

[14] N. Vata, T. Rudolph, and S. John, e-print quant-ph/9910046.

[15] B. Qiao and H.E. Ruda, J. Appl. Phys. **86**, 5237 (1999).

[16] D. Loss and D.P. DiVincenzo, Phys. Rev. A **57**, 120 (1998).

[17] G. Burkard, D. Loss, and D.P. DiVincenzo, Phys. Rev. B **59**, 2070 (1999).

[18] X. Hu and S. Das Sarma, Phys. Rev. A **61**, 062301 (2000).

[19] P. Zanardi and F. Rossi, Phys. Rev. Lett. **81**, 4752 (1998).

[20] A. Imamoglu, D.D. Awschalom, G. Burkard, D.P. DiVincenzo, D. Loss, M. Sherwin, and A. Small, Phys. Rev. Lett. **83**, 4204 (1999).

[21] S. Bandyopadhyay, Phys. Rev. B **61**, 13 813 (2000).

[22] T. Tanamoto, Phys. Rev. A **61**, 022305 (2000).

[23] T.A. Brun and H. Wang, Phys. Rev. A **61**, 032307 (2000).

[24] E. Biolatti, R.C. Iotti, P. Zanardi, and F. Rossi, Phys. Rev. Lett. **85**, 5647 (2000).

[25] B.E. Kane, Nature (London) **393**, 133 (1998).

[26] G.P. Berman, G.D. Doolen, P.C. Hammel, and V.I. Tsifrinovich, Phys. Rev. Lett. **86**, 2894 (2001).

[27] R. Vrijen, E. Yablonovitch, K. Wang, H.W. Jiang, A. Balandin, V. Roychowdhury, T. Mor, and D. DiVincenzo, Phys. Rev. A **62**, 012306 (2000).

[28] A. Shnirman, G. Schön, and Z. Hermon, Phys. Rev. Lett. **79**, 2371 (1997).

[29] L.B. Ioffe, V.B. Geshkenbeim, M.V. Feigel'man, A.L. Fauchère, and G. Blatter, Nature (London) **398**, 679 (1999).

[30] J.E. Mooij, T.P. Orlando, L. Levitov, L. Tian, C.H.v.d. Wal, and S. Lloyd, Science **285**, 1036 (1999).

[31] Y. Makhlin, G. Schön, and A. Shnirman, Comput. Phys. Commun. **127**, 156 (2000).

[32] A. Blais and A.M. Zagoskin, Phys. Rev. A **61**, 042308 (2000).

[33] P.M. Platzman and M.I. Dykman, Science **284**, 1967 (1999).

[34] R. Ionicioiu, G. Amaratunga, and F. Udrea, e-print quant-ph/9907043.

[35] A. Bertoni, P. Bordone, R. Brunetti, C. Jacoboni, and S. Reggiani, Phys. Rev. Lett. **84**, 5912 (2000).

[36] J.D. Franson, Phys. Rev. Lett. **78**, 3852 (1997).

[37] E. Knill, R. Laflamme, and G.J. Milburn, Nature (London) **409**, 46 (2001).

[38] V. Privman, I.D. Vagner, and G. Kventsel, Phys. Lett. A **239**, 141 (1998).

[39] A.Yu. Kitaev, e-print quant-ph/9707021.

[40] S. Lloyd, e-print quant-ph/0004010.

[41] H.E. Brandt, Prog. Quantum Electron. **22**, 257 (1998).

[42] D.P. DiVincenzo, Fortschr. Phys. **48**, 771 (2000).

[43] M. A. Nielsen and I. L. Chuang, *Quantum Computation and Quantum Information* (Cambridge University Press, Cambridge, UK, 2000).

[44] J. Preskill, Proc. R. Soc. London, Ser. A **454**, 385 (1998).

[45] A.P. Alivisatos, Science **271**, 933 (1996).

[46] L. Jacak, P. Hawrylak, and A. Wójs, *Quantum Dots* (Springer, Berlin, 1998).

[47] S.M. Maurer, S.R. Patel, C.M. Marcus, C.I. Duruoz, and J.S. Harris, Jr., Phys. Rev. Lett. **83**, 1403 (1999).

[48] N.H. Bonadeo, J. Erland, D. Gammon, D. Park, D.S. Katzer, and D.G. Steel, Science **282**, 1473 (1998).

[49] Al.L. Efros and A.L. Efros, Sov. Phys. Semicond. **16**, 772 (1982).

[50] L.E. Brus, J. Chem. Phys. **80**, 4403 (1984).

[51] A.I. Ekimov, A.A. Onushchenko, A.G. Plukhin, and Al.L. Efros, Sov. Phys. JETP **61**, 891 (1985).

[52] J.B. Xia, Phys. Rev. B **40**, 8500 (1989).

[53] Y.Z. Hu, M. Lindberg, and S.W. Koch, Phys. Rev. B **42**, 1713 (1990).

[54] K.J. Vahala and P.C. Sercel, Phys. Rev. Lett. **65**, 239 (1990).

[55] P.C. Sercel and K.J. Vahala, Phys. Rev. B **42**, 3690 (1990).

[56] A.I. Ekimov, F. Hache, M.C. Schanne-Klein, D. Ricard, C. Flytzanis, I.A. Kudryavtsev, T.V. Yazeva, A.V. Rodina, and Al.L. Efros, J. Opt. Soc. Am. B **10**, 100 (1993).

[57] T. Takagahara, Phys. Rev. B **47**, 4569 (1993).

[58] Al.L. Efros, Phys. Rev. B **46**, 7448 (1992).

[59] Al.L. Efros and A.V. Rodina, Phys. Rev. B **47**, 10 005 (1993).

[60] Al.L. Efros, M. Rosen, M. Kuno, M. Nirmal, D.J. Norris, and M. Bawendi, Phys. Rev. B **54**, 4843 (1996).

[61] D.J. Norris, Al.L. Efros, M. Rosen, and M.G. Bawendi, Phys. Rev. B **53**, 16 347 (1996).

[62] M.S. Hybertsen, Phys. Rev. Lett. **72**, 1514 (1994).

[63] M. Nirmal, D.J. Norris, M. Kuno, M.G. Bawendi, Al.L. Efros, and M. Rosen, Phys. Rev. Lett. **75**, 3728 (1995).

[64] M.E. Schmidt, S.A. Blanton, M.A. Hines, and P. Guyot-Sionnest, Phys. Rev. B **53**, 12 629 (1996).

[65] U. Banin, C.J. Lee, A.A. Guzelian, A.V. Kadavanich, A.P. Alivisatos, W. Jaskolski, G.W. Bryant, Al.L. Efros, and M. Rosen, J. Chem. Phys. **109**, 2306 (1998).

[66] J.-B. Xia and J. Li, Phys. Rev. B **60**, 11 540 (1999).

[67] J. Li and J.-B. Xia, Phys. Rev. B **61**, 15 880 (2000).

[68] Y. Wang and N. Herron, Phys. Rev. B **42**, 7253 (1990).

[69] P.E. Lippens and M. Lannoo, Phys. Rev. B **41**, 6079 (1990).

[70] H.H. von Grunberg, Phys. Rev. B **55**, 2293 (1997).

[71] N.A. Hill and K.B. Whaley, Phys. Rev. Lett. **75**, 1130 (1995).

[72] N.A. Hill and K.B. Whaley, Chem. Phys. **210**, 117 (1996).

[73] K. Leung, S. Pokrant, and K.B. Whaley, Phys. Rev. B **57**, 12 291 (1998).

[74] K. Leung and K.B. Whaley, Phys. Rev. B **56**, 7455 (1997).

[75] M.V. Rama Krishna and R.A. Friesner, Phys. Rev. Lett. **67**, 629 (1991).

[76] M.V. Rama Krishna and R.A. Friesner, J. Chem. Phys. **95**, 8309 (1991).

[77] L.-W. Wang and A. Zunger, J. Phys. C **98**, 2158 (1994).

[78] L.W. Wang and A. Zunger, Phys. Rev. B **53**, 9579 (1996).

[79] E. Rabani, B. Hetényi, B.J. Berne, and L.E. Brus, J. Chem. Phys. **110**, 5355 (1999).

[80] B. Delley and E.F. Steigmeier, Appl. Phys. Lett. **67**, 2370 (1995).

[81] G.T. Einevoll, Phys. Rev. B **45**, 3410 (1992).

[82] U.E.H. Laheld and G.T. Einevoll, Phys. Rev. B **55**, 5184 (1997).

[83] Y. Ohfuti and K. Cho, J. Lumin. **70**, 203 (1996).

[84] D.J. Norris and M.G. Bawendi, Phys. Rev. B **53**, 16 338 (1996).

[85] S.A. Empedocles and M.G. Bawendi, Science **278**, 2114 (1997).

[86] A.I. Ekimov, J. Lumin. **70**, 1 (1996).

[87] M. Lannoo, C. Delerue, and G. Allan, J. Lumin. **70**, 170 (1996).

[88] S.A. Empedocles, R. Neuhauser, K. Shimizu, and M.G. Bawendi, Adv. Mater. **11**, 1243 (1999).

[89] A.P. Alivisatos, K.P. Johnson, X. Peng, T.E. Wilson, C.J. Loweth, M.P. Bruchez, and P.G. Schultz, Nature (London) **382**, 609 (1996).

[90] M. Kuno, J.K. Lee, B.O. Daboussi, C.V. Mikulec, and M.G. Bawendi, J. Chem. Phys. **106**, 9869 (1997).

[91] H. Heckler, D. Kovalev, G. Polisski, N.N. Zinovev, and F. Koch, Phys. Rev. B **60**, 7718 (1999).

[92] A.M. Childs and I.L. Chuang, Phys. Rev. A **63**, 012306 (2001).

[93] C. Monroe, D. Leibfried, B.E. King, D.M. Meekhof, W.M. Itano, and D.J. Wineland, Phys. Rev. A **55**, R2489 (1997).

[94] H. Haken and H.C. Wolf, *Molecular Physics and Elements of Quantum Chemistry* (Springer, Berlin, 1995).

[95] K. Leung and K.B. Whaley, Phys. Rev. B **56**, 7455 (1997).

[96] N. Nishiguchi, Y. Ando, and N.M. Wybourne, J. Phys.: Condens. Matter **9**, 5751 (1997).

[97] L. D. Landau and E. M. Lifshitz, *Theory of Elasticity*, Course of Theoretical Physics Vol. 7 (Butterworth Heinemann, Oxford, 1998).

[98] M. O. Scully and M. S. Zubairy, *Quantum Optics* (Cambridge University Press, Cambridge, 1997).

[99] I. Murray Sargent and P. Horowitz, Phys. Rev. A **13**, 1962 (1976).

[100] T. Takagahara, J. Lumin. **70**, 129 (1996).

[101] U. Banin, G. Cerullo, A.A. Guzelian, C.J. Bardeen, A.P. Alivisatos, and C.V. Shank, Phys. Rev. B **55**, 7059 (1997).

[102] L.-M. Duan and G.-C. Guo, Phys. Rev. Lett. **79**, 1953 (1997).

[103] P. Zanardi and M. Rasetti, Phys. Rev. Lett. **79**, 3306 (1997).

[104] D.A. Lidar, I.L. Chuang, and K.B. Whaley, Phys. Rev. Lett. **81**, 2594 (1998).

[105] P. R. Bunker and P. Jensen, *Molecular Symmetry and Spectroscopy* (NRC Research Press, Ottawa, 1998).

[106] M. E. Rose, *Elementary Theory of Angular Momentum* (Dover, New York, 1995).

[107] J.-S. Peng, G.-X. Li, Peng Zhou, and S. Swain, Phys. Rev. A **61**, 063807 (2000).

[108] R. Lifshitz and M.L. Roukes, Phys. Rev. B **61**, 5600 (2000).

[109] K. Schwab, J.L. Arlett, J.M. Worlock, and M.L. Roukes, Physica B **6**, 60 (2001).

[110] A. Steane, C.F. Roos, D. Stevens, A. Mundt, D. Leibfried, F. Schmidt-Kaler, and R. Blatt, Phys. Rev. A **62**, 042305 (2000).

[111] D. Jonathan, M. Plenio, and P. Knight, Phys. Rev. A **62**, 042307 (2000).

[112] I. Broser *et al.*, in *Landolt-Bornstein: Numerical Data and Functional Relationships in Science and Technology,* edited by O. Madelung (Springer-Verlag, Berlin, 1994), Group III, Vol. 17b.

[113] A.M. Kapitonov, A.P. Stupack, S.V. Gaponenko, E.P. Petrov, A.L. Rogach, and A. Eychmuller, J. Phys. Chem. B **103**, 10109 (1999).

[114] K. Leung and K.B. Whaley, J. Chem. Phys. **110**, 11012 (1999).

[115] K. R. Brown and K.B. Whaley (unpublished).

[116] M. Shim and P. Guyot-Sionnest, Nature (London) **407**, 981 (2000).

[117] G.B. Grigoryan, E.M. Kazaryan, Al.L. Efros, and T.V. Yazeva, Sov. Phys. Solid State **32**, 1031 (1990).